

1 **Sinuuous Ridges in Chukhung Crater, Tempe Terra, Mars:**
2 **Implications for Fluvial, Glacial, and Glaciofluvial Activity.**

3 Frances E. G. Butcher^{1,2}, Matthew R. Balme¹, Susan J. Conway³, Colman Gallagher^{4,5}, Neil
4 S. Arnold⁶, Robert D. Storrar⁷, Stephen R. Lewis¹, Axel Hagermann⁸, Joel M. Davis⁹.

5 ¹ School of Physical Sciences, The Open University, Walton Hall, Milton Keynes, MK7
6 6AA, UK.

7 ² Current address: Department of Geography, The University of Sheffield, Sheffield, S10
8 2TN, UK (f.butcher@sheffield.ac.uk).

9 ³ CNRS, UMR 6112 Laboratoire de Planétologie et Géodynamique, Université de Nantes,
10 France

11 ⁴ UCD School of Geography, University College Dublin, Dublin 4, Ireland

12 ⁵ UCD Earth Institute, University College Dublin, Dublin 4, Ireland

13 ⁶ Scott Polar Research Institute, University of Cambridge, Cambridge, CB2 1ER, UK

14 ⁷ Department of the Natural and Built Environment, Faculty of Social Sciences and
15 Humanities, Sheffield Hallam University, Sheffield, S1 1WB, UK

16 ⁸ Biological and Environmental Sciences, University of Stirling, Stirling, FK9 4LA, UK

17 ⁹ Department of Earth Sciences, Natural History Museum, London, UK.

18

19 **Keywords**

20 Mars, glaciation; Mars, fluvial; Sinuous ridges; Eskers; Inverted paleochannels.

21 **Abstract**

22 We present a geomorphic map of Chukhung crater (38.47°N, 72.42°W) in central Tempe
23 Terra, Mars. Chukhung crater formed ~3.6–2.1 Ga, between the early Hesperian and early
24 Amazonian periods of Mars' geologic history. It hosts dendritic networks of crater wall
25 valleys, broad crater floor valleys, mid-to-late-Amazonian-aged debris-covered glaciers,
26 moraine-like deposits, and a radial assemblage of sinuous ridge landforms. We explore the
27 origins of landforms in Chukhung crater, focusing in particular upon the sinuous ridges. In
28 northern Chukhung crater, sinuous ridges extend downslope from fluvial valley systems on
29 the northern crater wall. We interpret the northern sinuous ridges as inverted paleochannels:
30 ridges formed by exhumation of resistant and/or indurated fluvial channel fill deposits. The
31 origins of sinuous ridges on the southern floor of Chukhung crater are more ambiguous. They
32 emerge from beneath moraine-like ridges which bound extant debris-covered glaciers
33 extending from the southern wall of the crater. The southern sinuous ridges have numerous
34 morphological and contextual similarities to eskers: ridges of glaciofluvial sediment
35 deposited in meltwater conduits within or beneath wet-based glaciers. The close proximity of
36 the northern and southern sinuous ridges, however, calls into question an interpretation which
37 ascribes a different origin to each set. The similarity in the overarching process between esker
38 and inverted channel formation (i.e., exposure by the removal of a bounding medium, be that
39 ice or sediments/rock) results in convergence of form between eskers and inverted
40 paleochannels. We discuss the esker-like characteristics of the southern sinuous ridges in
41 detail, and argue that one of two ridge populations in southern Chukhung crater is best
42 explained by the esker hypothesis while the other could be explained under either the esker or
43 the inverted paleochannel hypothesis. Regardless of the specific formation mechanism for the
44 southern sinuous ridges, we find that Chukhung crater has undergone significant modification
45 by liquid water since its formation. The northern sinuous ridges and associated crater-wall

46 valleys provide evidence for subaerial drainage of precipitation and/or snowmelt. This
47 suggests that Chukhung crater, and possibly the surrounding region, experienced unusually
48 warm and wet episodes between the early Hesperian and mid Amazonian. If some or all of
49 the southern sinuous ridges are eskers, they could provide evidence for an additional
50 influence of glacial meltwater in Chukhung crater during the mid-to-late Amazonian. If wet-
51 based glaciation did occur in Chukhung crater, the location of the crater between major
52 branches of the Tempe Fossae tectonic rift system would add to the growing body of
53 evidence that elevated geothermal heat flux was an important driver of localized occurrences
54 of recent wet-based glaciation on Mars.

55 **1. Introduction**

56 Evidence for past melting of putative debris-covered glaciers (viscous flow features, VFFs) in
57 Mars' mid-latitudes is extremely rare. Recently, however, candidate eskers have been
58 identified in association with two late-Amazonian-aged VFFs in Phlegra Montes (Gallagher
59 and Balme, 2015) and NW Tempe Terra (Butcher et al., 2017, 2020). Eskers are sinuous
60 ridges of glaciofluvial sediment deposited by meltwater draining through tunnels within
61 glacial ice.

62 The locations of the Phlegra Montes and NW Tempe Terra eskers within tectonic rift/graben
63 valleys supports the hypothesis that localized geothermal heating, possibly accompanied by
64 viscous strain heating within the basal ice, was a prerequisite for the production of glacial
65 meltwater under cold late-Amazonian climate conditions (Gallagher and Balme, 2015;
66 Butcher et al., 2017). Recent modeling experiments exploring the environmental conditions
67 required to explain a possible present-day subglacial lake beneath Mars' south polar ice cap
68 (Orosei et al., 2018) also conclude that above-average geothermal heat flux is required for
69 basal melting (Arnold et al., 2019; Sori and Bramson, 2019).

70 In order to explore the geothermal hypothesis further, and to constrain the possible extent of
71 wet-based glaciation on Amazonian Mars, it is necessary to search for additional candidate
72 eskers associated with extant VFFs elsewhere on Mars. In this study, we present Chukhung
73 crater in central Tempe Terra (38.47°N, 72.42°W; Figure 1) as a new site of interest in this
74 search. Chukhung crater hosts sinuous ridges with many esker-like characteristics, which
75 emerge from extant, mid- to late-Amazonian-aged VFF. However, it also hosts landforms
76 interpreted as inverted fluvial paleochannels, which could cast doubt on the origin of the
77 VFF-linked ridges as eskers because of the issue of convergence of form (whereby different
78 processes produce landforms with similar morphologies) between inverted paleochannels and
79 eskers (e.g., Burr et al., 2009). Inverted paleochannels are ridges which preserve fluvial
80 channels in positive relief; they form when channel-fill deposits develop greater resistance to
81 erosion than the adjacent valley floor and/or sides (e.g., by chemical induration and/or
82 armoring), and are exhumed by preferential erosion of those neighboring materials (Maizels,
83 1987; Pain and Oilier, 1995; Williams et al., 2007, 2013). Unlike eskers, their formation does
84 not require glaciation or glacial meltwater.

85 We present geomorphic analysis of landforms within Chukhung crater, which is early
86 Hesperian to early Amazonian in age. We draw inferences about the processes that have
87 modified its interior, including fluvial, glacial, and possibly glaciofluvial processes.
88 However, we demonstrate that the interpretation of glacier-linked sinuous ridges in southern
89 Chukhung crater as eskers, and hence the possibility that glaciers in Chukhung crater
90 produced meltwater, is cast into doubt by their coexistence with inverted paleochannels. We
91 do, however, identify one population of sinuous ridges in southern Chukhung crater which is
92 better explained under the esker hypothesis than under the inverted paleochannel hypothesis.
93 Chukhung crater provides a cautionary tale that should be considered during the search for
94 eskers elsewhere on Mars.

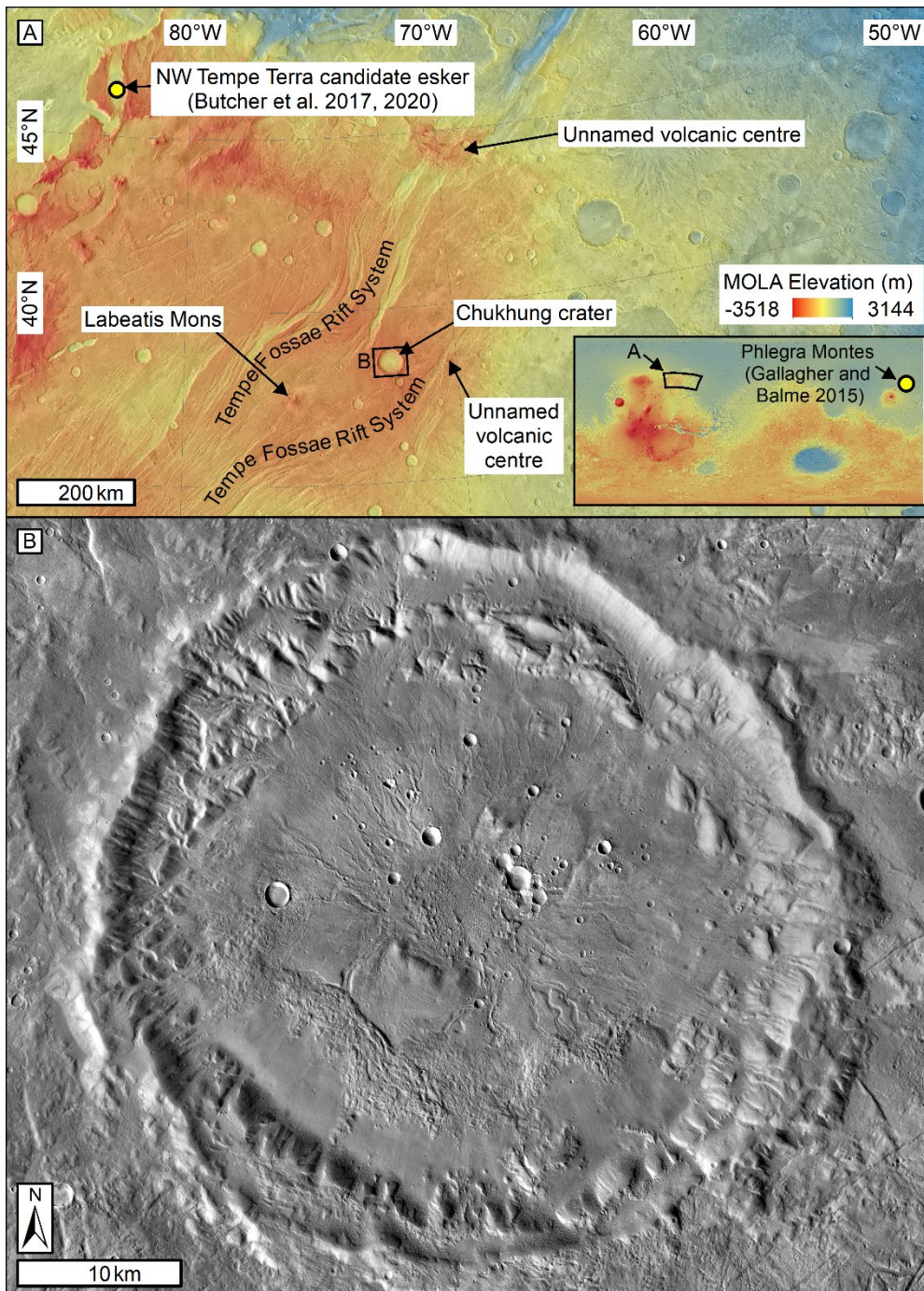


Figure 1. Location of Chukhung crater. (A) Thermal Emission Imaging System (THEMIS; Christensen et al. 2004; Edwards et al. 2011) daytime infrared image mosaic overlain by colorized Mars Orbiter Laser Altimeter (MOLA; Smith et al. 2001) elevation map of central Tempe Terra (location A in inset global MOLA map), showing the location of Chukhung crater relative to major fault branches and volcanic centers of the Tempe Fossae rift system. Yellow points show locations of candidate glacier-linked eskers previously studied by Butcher et al. (2017, 2020) in NW Tempe Terra, and by Gallagher and Balme (2015) in Phlegra Montes. (B) Context camera image mosaic of Chukhung crater. Extent shown in panel A. See Table S1 for a list of data products.

96 Regardless of whether the sinuous ridges are eskers or inverted paleochannels, however, we
97 demonstrate that Chukhung crater has undergone multiple episodes of modification by liquid
98 water since its formation between the early Hesperian and early Amazonian (~3.6–2.1 Ga),
99 and possibly as recently as the mid- to late-Amazonian when environmental conditions on
100 Mars are generally thought to have been extremely cold and hyper-arid.

101 **2. Study Location: Chukhung Crater**

102 Chukhung crater (38.47°N, 72.42°W) is a ~45 km diameter, ~2.3 km deep impact crater in
103 central Tempe Terra (Figure 1). It is within the same physiographic region as the tectonic rift
104 valley in NW Tempe Terra that hosts the candidate glacier-linked esker identified by Butcher
105 et al. (2017), which is ~600 km to the northwest. Chukhung crater is located between major
106 grabens within the southwestern segment of the Tempe Fossae rift system (Hauber and
107 Kronberg, 2001), and ~150 km ENE of the central construct of Labeatis Mons. Labeatis
108 Mons is a ~200 km diameter, late-Hesperian-aged (3.51 Ga; Hauber and Kronberg, 2001)
109 volcano which formed during late-stage rifting in Tempe Fossae, and was probably active
110 after major rifting ceased (Hauber and Kronberg, 2001; Hauber et al., 2010). A second,
111 smaller volcanic construct is located within a swarm of grabens ~70 km east of Chukhung
112 crater (Figure 1A).

113 **3. Aims**

114 We present a geomorphic map of Chukhung crater and explore hypotheses for the formation
115 of its interior units and landforms. In particular, we explore the origins of sinuous ridges that
116 occupy two different portions of the crater floor: (1) sinuous ridges on the southern portion of
117 the crater floor that are spatially associated with (and commonly emerge from beneath) VFF-
118 terminal deposits, and (2) sinuous ridges that extend across the northern portion of the crater
119 floor where there is no discernible evidence for past or present glaciation.

120 We first consider the hypotheses that: (1) the VFF-linked ridges on the southern portion of
121 the crater floor are eskers, and (2) that the sinuous ridges on the northern portion of the crater
122 floor are inverted paleochannels of non-glacial origin. We then discuss various alternative
123 hypotheses for the origins of the sinuous ridges: (1) that both populations of sinuous ridges in
124 Chukhung crater are eskers, (2) that both populations are inverted paleochannels which pre-
125 date the present glaciation of Chukhung crater, or (3) that the northern and southern sinuous
126 ridge populations contain mixtures of eskers and inverted paleochannels, and thus that the
127 formation mechanisms cannot be divided on a north-south basis. In considering the
128 alternative formation hypotheses for the sinuous ridges, we highlight some of the challenges
129 that remain for the ongoing search for eskers on Mars. Finally, we consider the implications
130 of the sinuous ridges for the history of fluvial, glacial, and glaciofluvial activity in Chukhung
131 crater.

132 **4. Data and Methods**

133 4.1 Observations and Mapping

134 We produced a geomorphic map of the interior of Chukhung crater using a basemap
135 comprising ~6 m/pixel Context Camera (CTX; Malin et al., 2007) images (listed in Table
136 S1), which provide complete coverage of the mapping area (Figure 2). We supplemented our
137 analyses with seven High Resolution Imaging Science Experiment (HiRISE; McEwen et al.,
138 2007) images (six of 25 cm/pixel, and one of 50 cm/pixel horizontal resolution), which
139 provide partial coverage of the mapping area (Figure 2). We integrated these image data with:
140 (1) a single 75 m/pixel High Resolution Stereo Camera (HRSC; Neukum et al., 2004;
141 Jaumann et al., 2007) digital elevation model (DEM), which provides complete coverage of
142 the mapping area (Figure 2, Table S1); (2) a 24 m/pixel DEM derived from two CTX images
143 by Mayer and Kite (2016), which provides coverage of the western two-thirds of the mapping

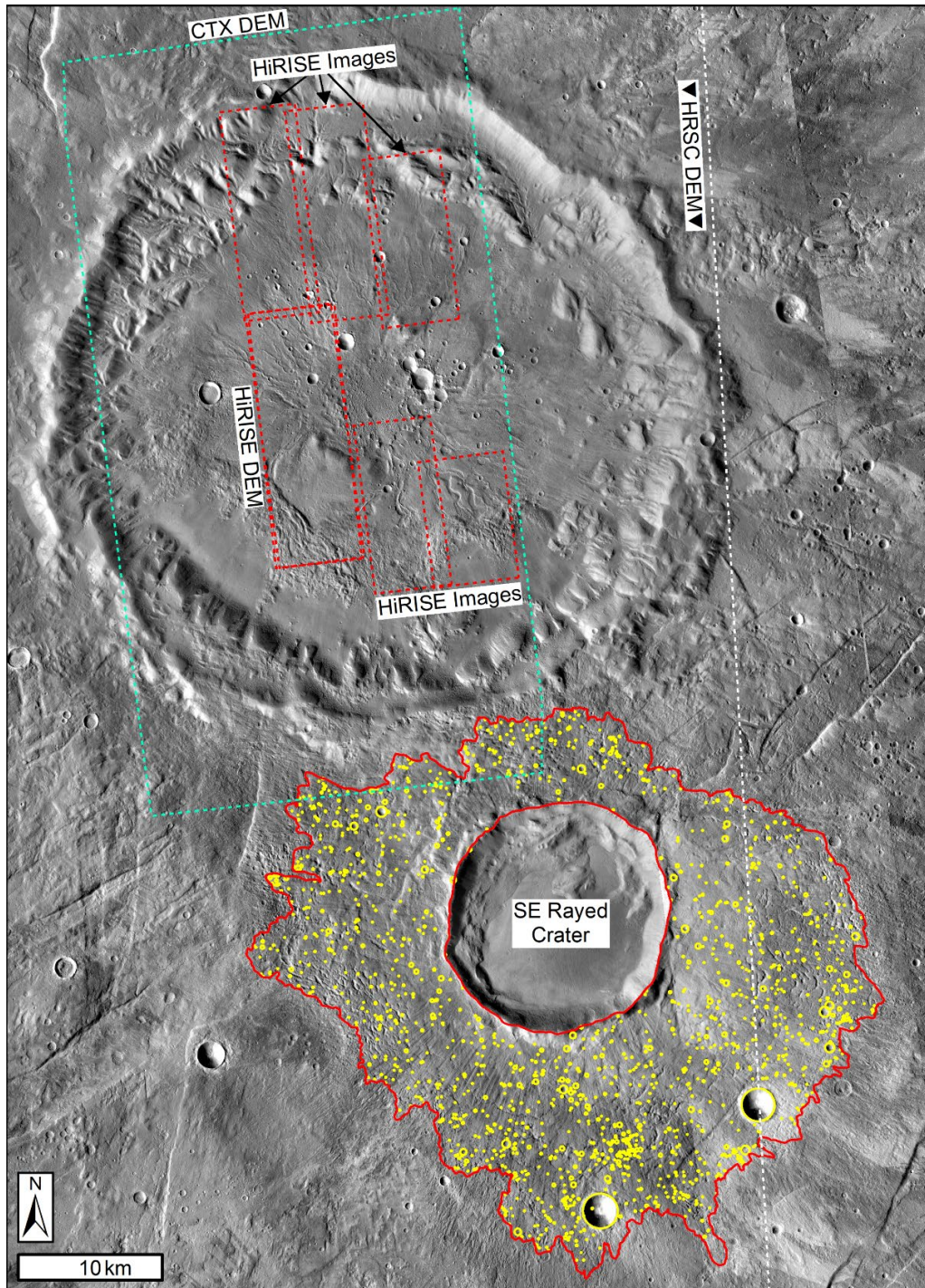


Figure 2. Data coverage of Chukhung crater and the rayed impact crater to the SE. The CTX image basemap provides complete coverage of the study area. Dashed boxes show extent of: 7 HiRISE images (red), including a stereo pair from which Mayer and Kite (2016) produced a digital elevation model; the CTX DEM (blue) from Mayer and Kite (2016); and the HRSC DEM (white dashed line shows easternmost extent). The solid red line shows the area of the impact ejecta of the SE rayed crater for which we obtained impact crater size-frequency statistics. Yellow circles are counted impact craters with diameters >70 m. See Table S1 for data products.

145 area; and (3) a 1 m/pixel HiRISE DEM generated by the same authors (Mayer and Kite,
146 2016), which provides coverage of a portion of the central crater floor (see Table S1 for a
147 complete list of data products, and Figure 2 for a map of data coverage). To minimize
148 cartographic distortion, we digitized the map in a sinusoidal projection centered on 72.5°W
149 using ESRI ArcGIS 10.1 software.

150 We identified map units based on visual similarities in their surface morphologies. We
151 identified contacts between map units based on changes in surface morphology and/or
152 differences in unit emplacement ages evidenced by superposition relationships.

153 4.2 Age Estimations from Impact Crater Size-Frequency Distributions

154 We measured size-frequency distributions of impact craters to estimate: (1) an approximate
155 envelope for the age of Chukhung crater itself, and (2) the minimum age of the VFF within
156 Chukhung crater. We measured crater size-frequency distributions on the CTX image
157 basemap using the *CraterTools* add-in for ArcGIS (Kneissl et al., 2011).

158 The interior of Chukhung crater has been subject to significant post-impact modification such
159 that impact crater populations within it would not provide a reliable estimation of the age of
160 the Chukhung-forming impact. Additionally, the ejecta blanket of Chukhung crater is thin
161 and indistinct such that age determinations based on the size-frequency distribution of impact
162 craters upon it would be unreliable. Therefore, we constrained an approximate envelope for
163 the age of Chukhung crater itself based on the modeled ages of units that underlie and
164 superpose it in the regional stratigraphy. We compared the estimated age of the early-
165 Hesperian volcanic unit (eHv; Tanaka et al., 2014a), upon which it is superposed, with new
166 measurements of the size-frequency distribution of impact craters on the better-preserved
167 ejecta of a ~15 km diameter rayed crater, which superposes the southeastern rim of
168 Chukhung crater (hereafter referred to as the ‘SE rayed crater’; Figure 2). The age estimate

169 for the early-Hesperian volcanic unit by Tanaka et al. (2014a) is based upon the size-
170 frequency distribution of impact craters on a reference surface in Icaria Planum centered on
171 105.96°W, 41.92°S. We measured all un-deformed impact craters of diameter (D) ≥ 70 m on
172 the surface of the ejecta blanket of the SE rayed crater (Figure 2). The decameter-scale relief
173 of the rayed ejecta made identification of impact craters with $D < 70$ m unreliable.

174 To estimate a minimum age for the VFF in Chukhung crater, we measured all un-deformed
175 impact craters of $D \geq 50$ m on their surfaces. Impact craters with $D < 50$ m could not be
176 distinguished reliably from pits on the VFF surfaces.

177 We identified potential for a significant influence of secondary impact craters from the SE
178 rayed crater upon the measured impact crater size-frequency distributions. Therefore, we
179 performed spatial randomness analyses on the measured impact crater populations using the
180 randomness analysis tool in *CraterStats2* (Michael et al., 2012). We produced 3000 random
181 spatial distributions of an impact crater population with the same characteristics as the
182 measured population. Following Michael et al. (2012), we then compared the mean second
183 closest neighbor distance (M2CND) of the measured population (for various ranges of impact
184 crater diameters) to those of the simulated populations (over the same diameter range). For
185 diameter ranges in which the true M2CND fell within one standard deviation of the mean
186 simulated M2CND, we considered crater distributions to be spatially random. For impact
187 crater diameter ranges in which the true M2CND deviated from the mean simulated M2CND
188 by more than one standard deviation, we considered impact craters to be non-randomly
189 distributed. Where this was true, we considered contamination of the impact crater population
190 by secondary impact craters to be important and approached interpretation of modeled ages
191 with greater caution. Secondary impact craters artificially increase the modeled age of an
192 affected surface. Spatially heterogeneous resurfacing processes can also cause spatial

193 clustering. In contrast to secondary cratering, resurfacing destroys impact craters, resulting in
194 underestimation of model ages from impact crater size-frequency distributions.

195 **5. Observations**

196 Our geomorphic map of Chukhung crater is displayed in Figure 3, and example images of
197 mapped units are displayed in Figure 4. An enlarged version of the map is provided in
198 Supplementary Figure S1. Chukhung crater is ~45 km in diameter and ~2.3 km deep. It has
199 multiple crater wall terraces, and a ~10.7 km diameter, ~225 m deep central floor pit
200 (Robbins and Hynek, 2012). The rim of the central pit has variable topographic expression
201 (Figure 5 and Figure 6). Steep scarps separate the NE and SW margins of the central pit from
202 the crater floor above (Figure 6), whereas the NW and eastern margins of the central pit are
203 topographically indistinct; topographic profiles from the crater rim to the floor of the central
204 pit in these locations (e.g., Figure 6) are broadly concave. The floor of Chukhung crater has
205 undergone significant post-impact modification. It hosts various geomorphic units (Figure 3–
206 Figure 6), which we now describe.

207 **5.1 Lobate Debris Aprons and Highland Mantling Units**

208 Deposits with pitted and lineated surface textures, consistent with lobate debris apron (LDA)
209 type VFFs (Squyres, 1979; Head et al., 2010), extend up to 5 km across the floor of
210 Chukhung crater from the W–SE portions of the crater wall (Figure 3, Figure 4C, Figure 5,
211 and Figure 8A). LDA are widely considered to be analogous to debris-covered glaciers (e.g.,
212 Holt et al., 2008; Plaut et al., 2009; Petersen et al., 2018). Topographic profiles oriented from
213 the headward margins to the termini of LDA in Chukhung crater are predominantly convex-
214 up (Figure 5), though in some areas they are concave. At their headward margins, the LDA
215 surfaces transition gradationally to a highland mantling unit (*Hmu* in Figure 3), similar to that
216 interpreted as ice-rich highland mantling in NW Tempe Terra by Butcher et al. (2017).

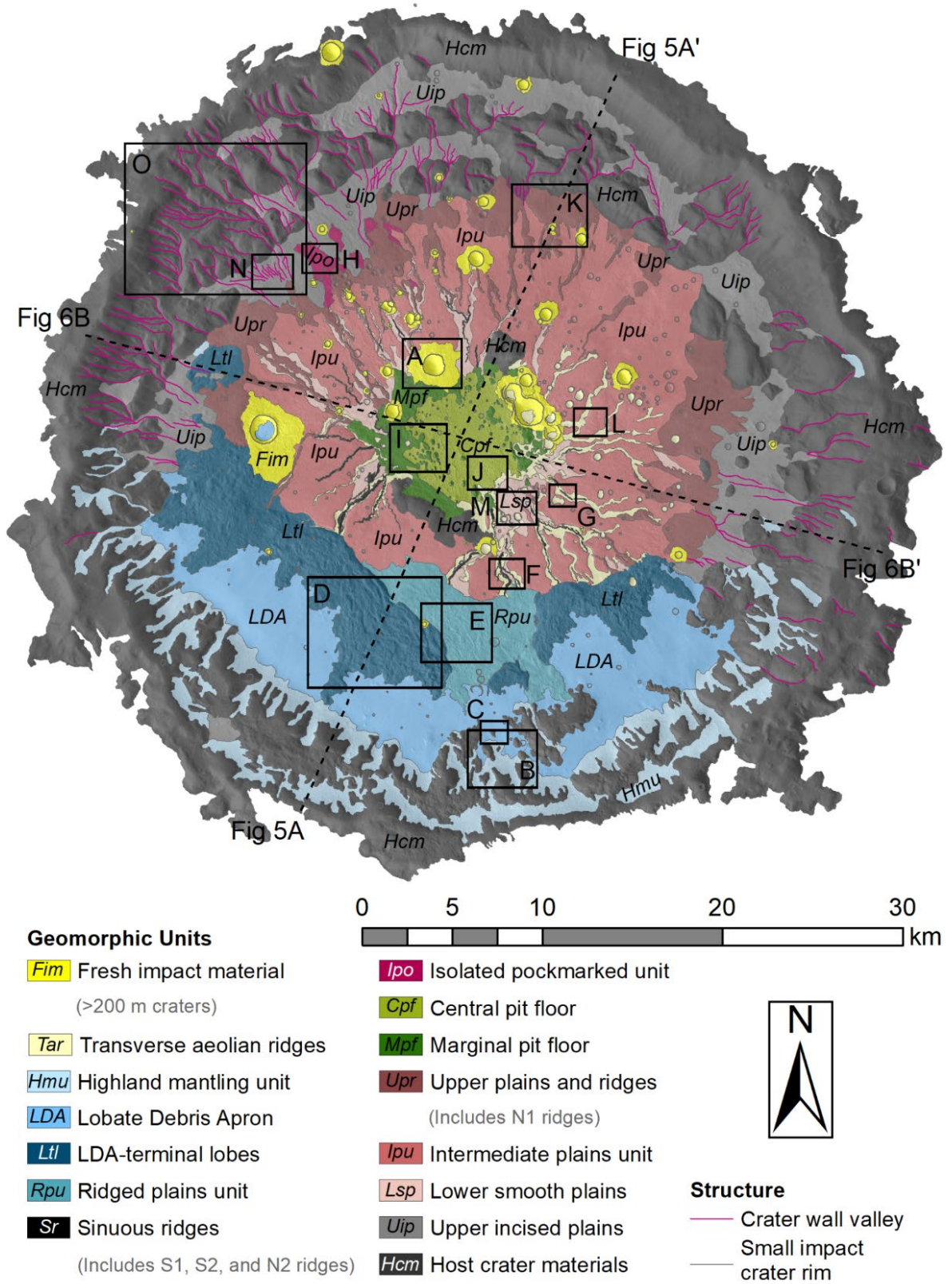


Figure 3. Geomorphologic map of Chukhung crater. Boxes show extents of panels in Figure 4, and dashed lines show locations of profiles in A–A’ and B–B’ in Figure 5 and Figure 6, respectively. Map overlain on CTX image mosaic (see Table S1). See Figure S1 for enlarged map.

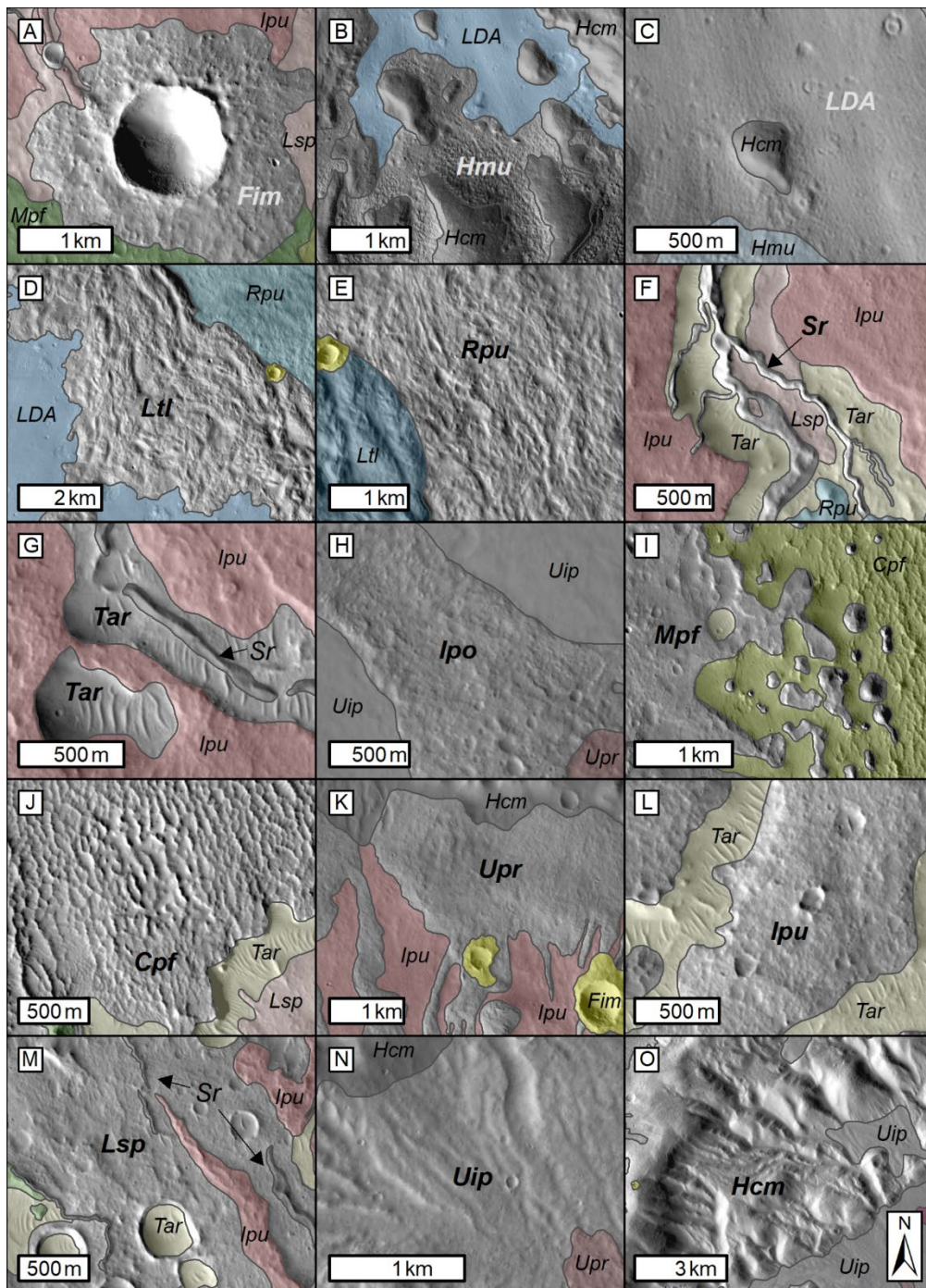
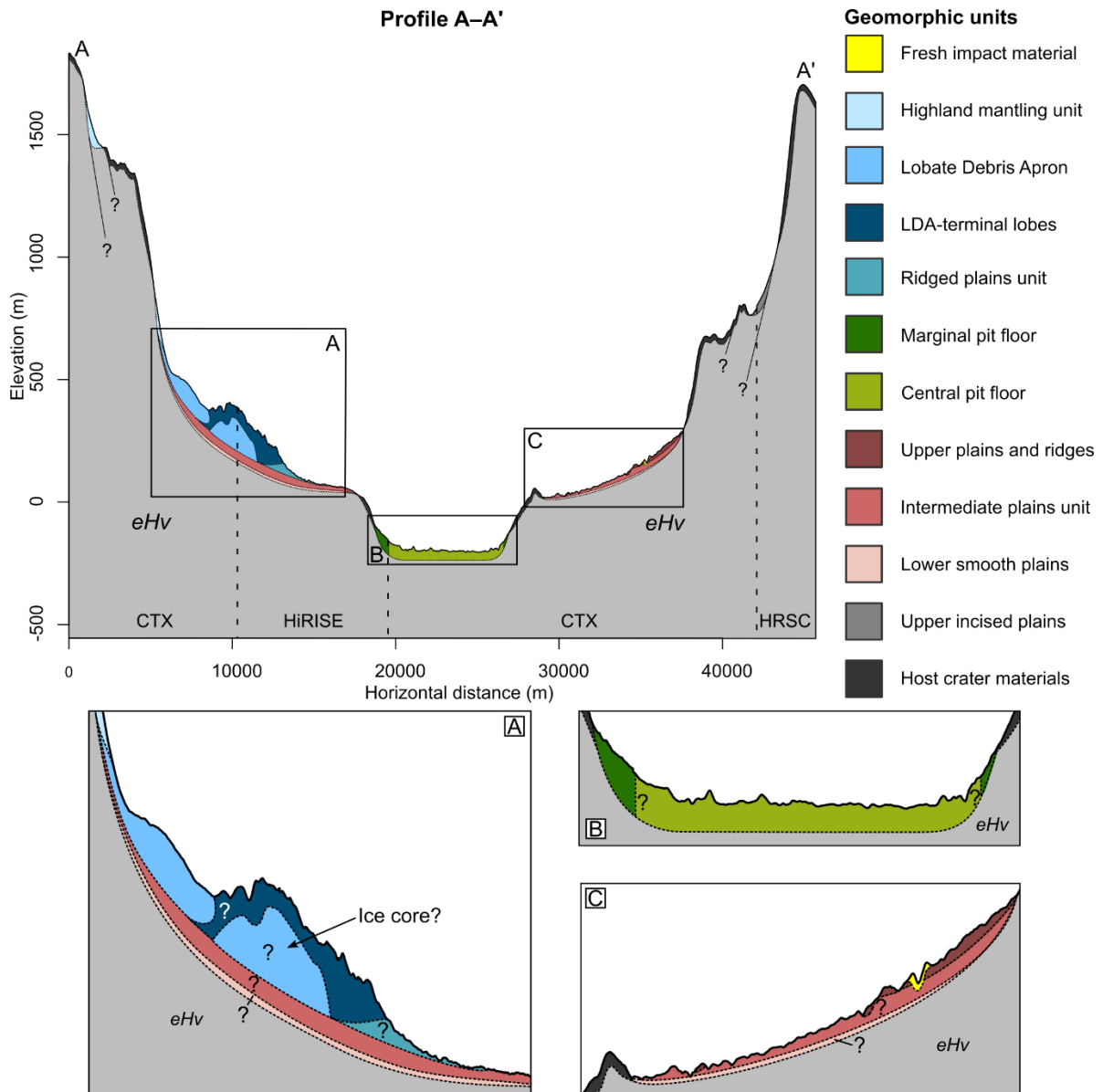


Figure 4. CTX images of geomorphic units in Chukhung crater. For clarity, contextual units are colored, but the subject unit of each panel (with unit label emboldened) is not. See Figure 3 for extents and legend. (A) Fresh impact material, *Fim*. (B) Highland mantling unit, *Hmu*. (C) Lobate Debris Apron, *LDA*. (D) LDA-terminal lobes, *Ltl*. (E) Ridged plains unit, *Rpu*. (F) Sinuous ridges, *Sr*. (G) Transverse aeolian ridges, *Tar*. (H) Isolated pockmarked unit, *Ipo*. (I) Marginal pit floor unit, *Mpf*. (J) Central pit floor, *Cpf*. (K) Upper plains and ridges unit, *Upr*. (L) Intermediate plains unit, *Ipu*. (M) Lower smooth plains, *Lsp*. (N) Upper incised plains, *Uip*. (O) Host crater materials, *Hcm*. See Table S1 for data products.



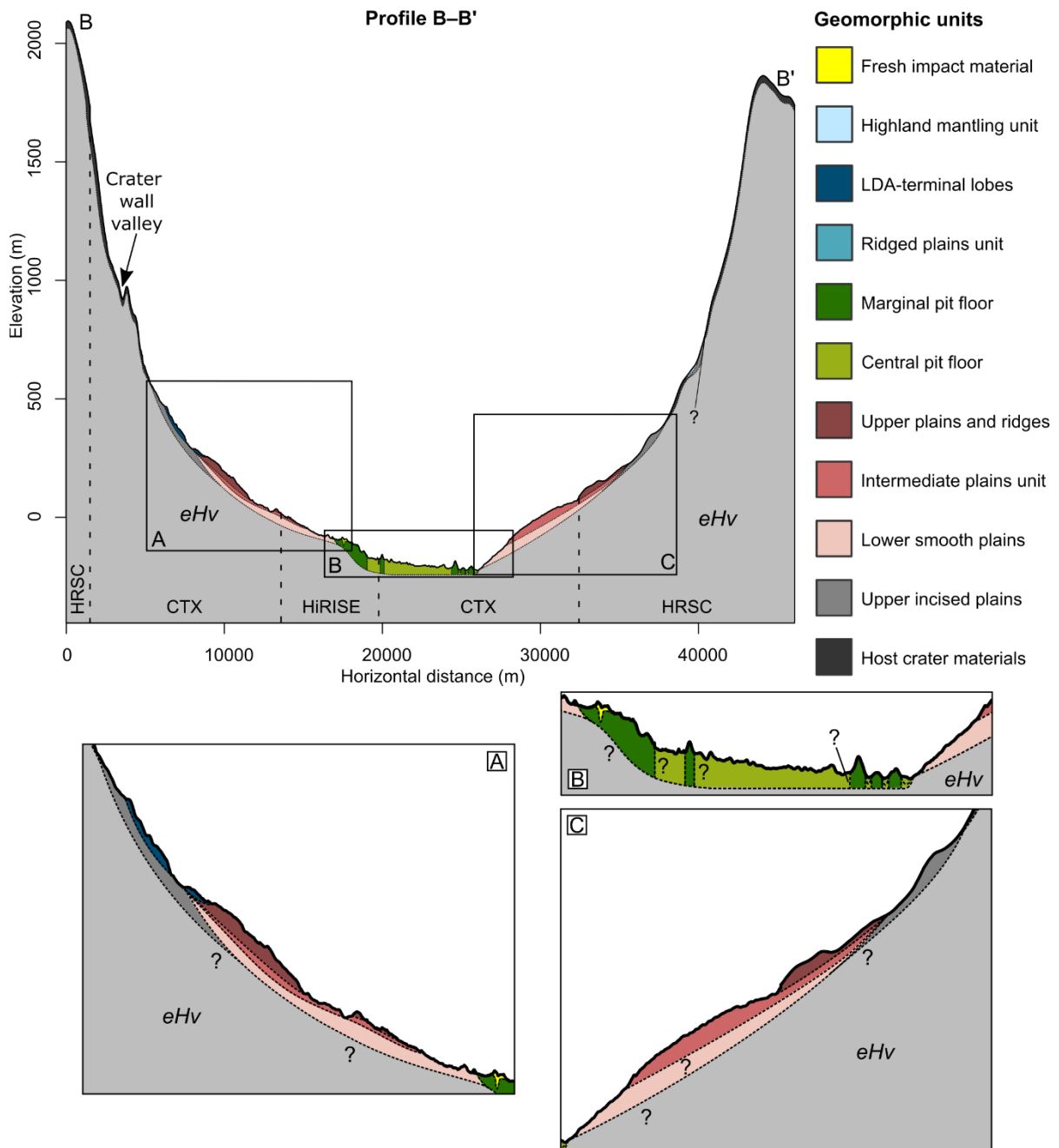
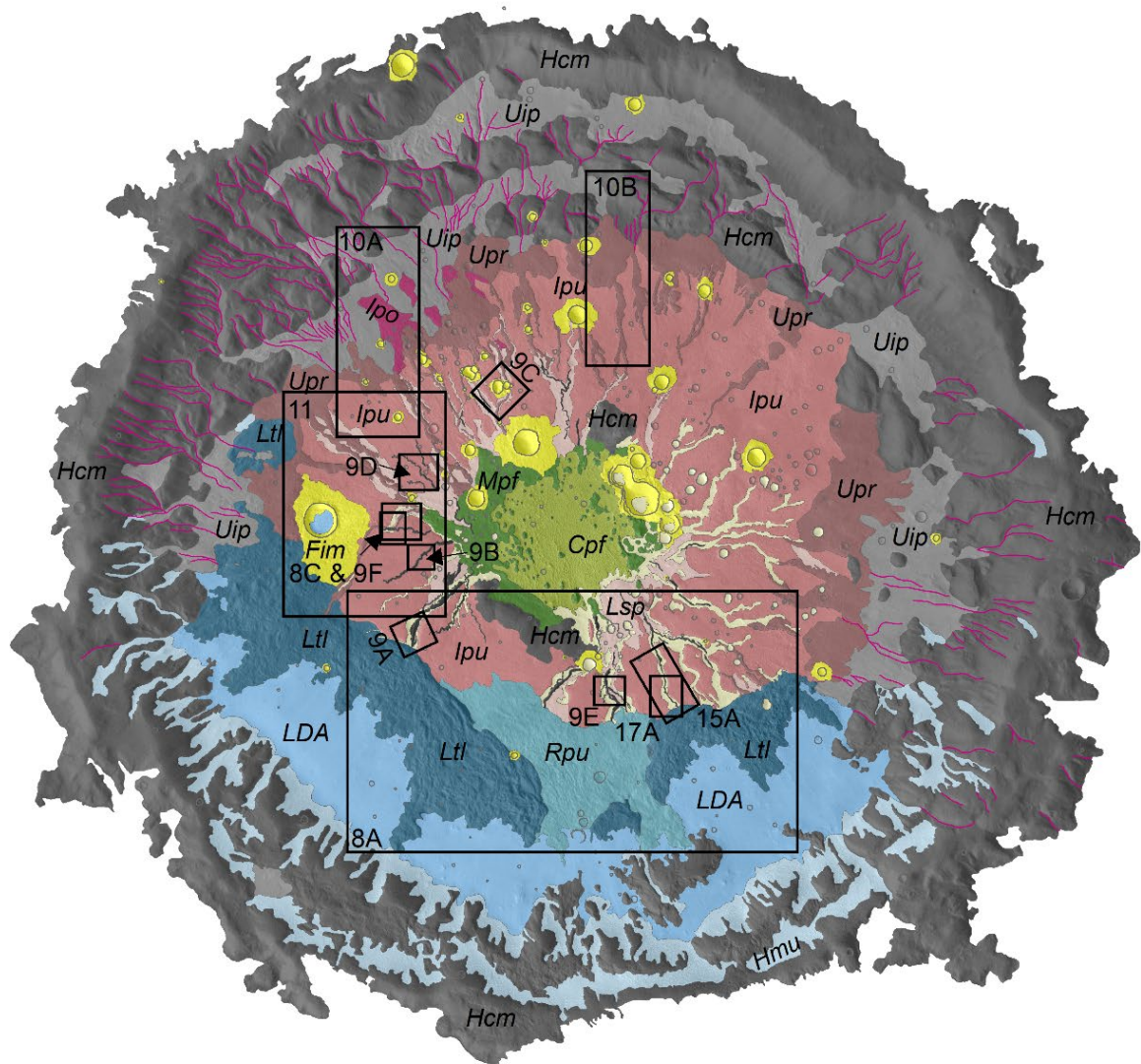


Figure 6. Schematic cross-section B–B’, showing inferred stratigraphic relationships between mapped units in Chukhung crater. Location of profile is shown in Figure 3. The upper solid line is topography from CTX, HiRISE, and HRSC DEMs at 15 times vertical exaggeration (dashed lines show DEM extents, see Table S1 for data products), and all contacts below this line have inferred depths and profiles. Boxes show extents of enlarged inset views A, B, and C. *eHv* is the early-Hesperian volcanic unit (Tanaka et al., 2014a, 2014b). In this profile, the NW margin of the central pit is not topographically prominent, resulting in a broadly concave profile from the NW crater wall to the center of the crater.



Geomorphic Units

- | | |
|--|--|
| Fim Fresh impact material
(>200 m craters) | Ipo Isolated pockmarked unit |
| Tar Transverse aeolian ridges | Cpf Central pit floor |
| Hmu Highland mantling unit | Mpf Marginal pit floor |
| LDA Lobate Debris Apron | Upr Upper plains and ridges
(Includes N1 ridges) |
| Ltl LDA-terminal lobes | Ipu Intermediate plains unit |
| Rpu Ridged plains unit | Lsp Lower smooth plains |
| Sr Sinuous ridges
(Includes S1, S2, and N2 ridges) | Uip Upper incised plains |
| | Hcm Host crater materials |



Structure

- Crater wall valley
- Small impact crater rim

Figure 7. Geomorphic map of Chukhung crater showing extents of subsequent figures. See Figure S1 for enlarged map.

222 The highland mantling unit has a lineated texture and infills topographic lows in the southern
223 crater wall, including wide (hundreds of meters), low-sinuosity crater wall valleys, and the
224 upper surfaces of crater wall terraces (Figure 3, Figure 4B, Figure 5, and Figure 6).

225 We do not observe similar ice-rich LDA or highland mantling deposits on the northern or
226 eastern portions of the crater floor or wall (Figure 3, Figure 5, and Figure 6).

227 5.2 LDA-Terminal Lobes and Ridged Plains Units

228 The termini of the LDAs in Chukhung crater are bounded by prominent lobate ridges (LDA-
229 terminal lobes, *Ltl*) comprising hummocky deposits and concentric parallel ridges (Figure 3,
230 Figure 4D, and Figure 8). The lobes are oriented parallel to the LDA termini and extend 2–
231 5 km across the southern crater floor. LDA materials infill topographic depressions in the
232 upper margins of the LDA-terminal lobes (Figure 8), whereas the steep lobe-frontal margins
233 have tens of meters (up to ~100 m) of relief (Figure 5). Two ~2 km wide gaps exist in the
234 lobate deposits at the termini of the north-facing LDA (Figure 3 and Figure 8). In these zones,
235 the LDA termini transition to low-relief hummocky plains (Figure 4E, Figure 5, and Figure
236 8A) comprising heterogeneous undulatory forms which superpose numerous parallel, NNW-
237 oriented lineae with lengths of hundreds of meters (Figure 4E). The LDA-terminal lobes and
238 ridged plains units occur only on the southern and western portions of the crater floor.

239 5.3 Southern Sinuous Ridges and Crater-Floor Valleys in Intermediate Plains

240 The southern floor of Chukhung crater hosts 16 sinuous ridge systems (Figure 8 and Figure
241 9A, B, E, and F), five of which emerge from beneath the LDA-terminal lobes and ridged
242 plains units (e.g., Figure 8A and D, and Figure 9A). They extend several kilometers towards
243 the margins of the crater's central pit. Superposition relationships (e.g., Figure 9E) suggest
244 that at least two stratigraphically-distinct sets of sinuous ridges exist on the southern crater

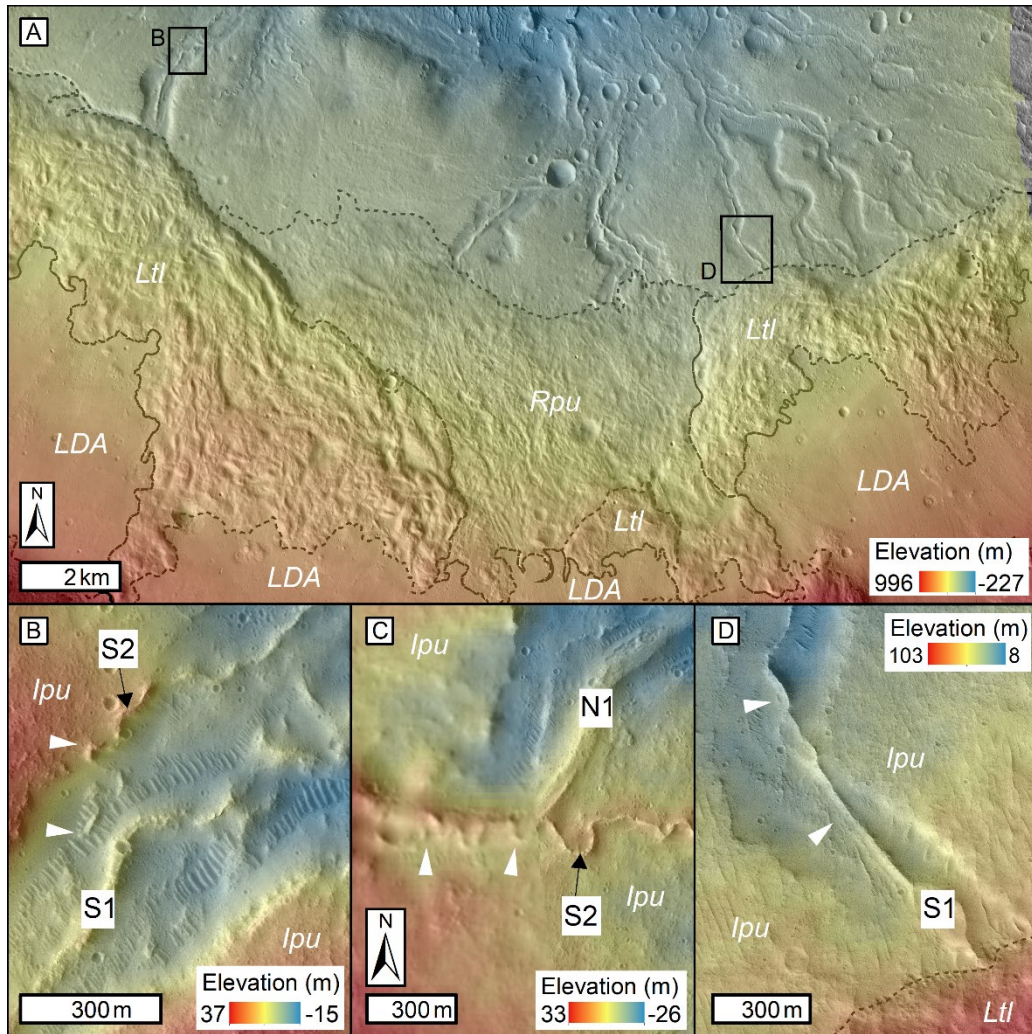


Figure 8. Landform associations and sinuous ridges on the southern floor of Chukhung crater.(A) CTX image mosaic overlain by 24 m/pixel CTX DEM showing the LDA-terminal lobes (*Ltl*) which bound the LDA termini, the ridged plains unit (*Rpu*) which occupies a gap in the *Ltl*, and the emergence of several of the southern sinuous ridges from beneath these units. Black boxes show the extents of panels B and D. (B) HiRISE image overlain by 1 m/pixel HiRISE DEM showing a sharp-crested S2-type ridge which weaves up and down the wall of a crater-floor valley (between white arrows) occupied by an S1-type ridge. (C) HiRISE and CTX images overlain by 24 m/pixel CTX DEM showing a sharp-crested S2-type ridge superposing the flat-topped crest of the SW branch of the N1-type ridge in Figure 11 (between white arrows) and ascends out of the crater floor valley and onto the adjacent intermediate plains (*Ipu*). Extent shown in Figure 7. (D) HiRISE image overlain by 24 m/pixel CTX DEM showing a sharp-crested S1-type ridge which emerges from beneath the LDA-terminal lobe (*Ltl*) unit and appears to ascend then descent the wall of the crater floor valley it occupies (between white arrows) rather than following the strike of the valley floor. See Table S1 for data products.

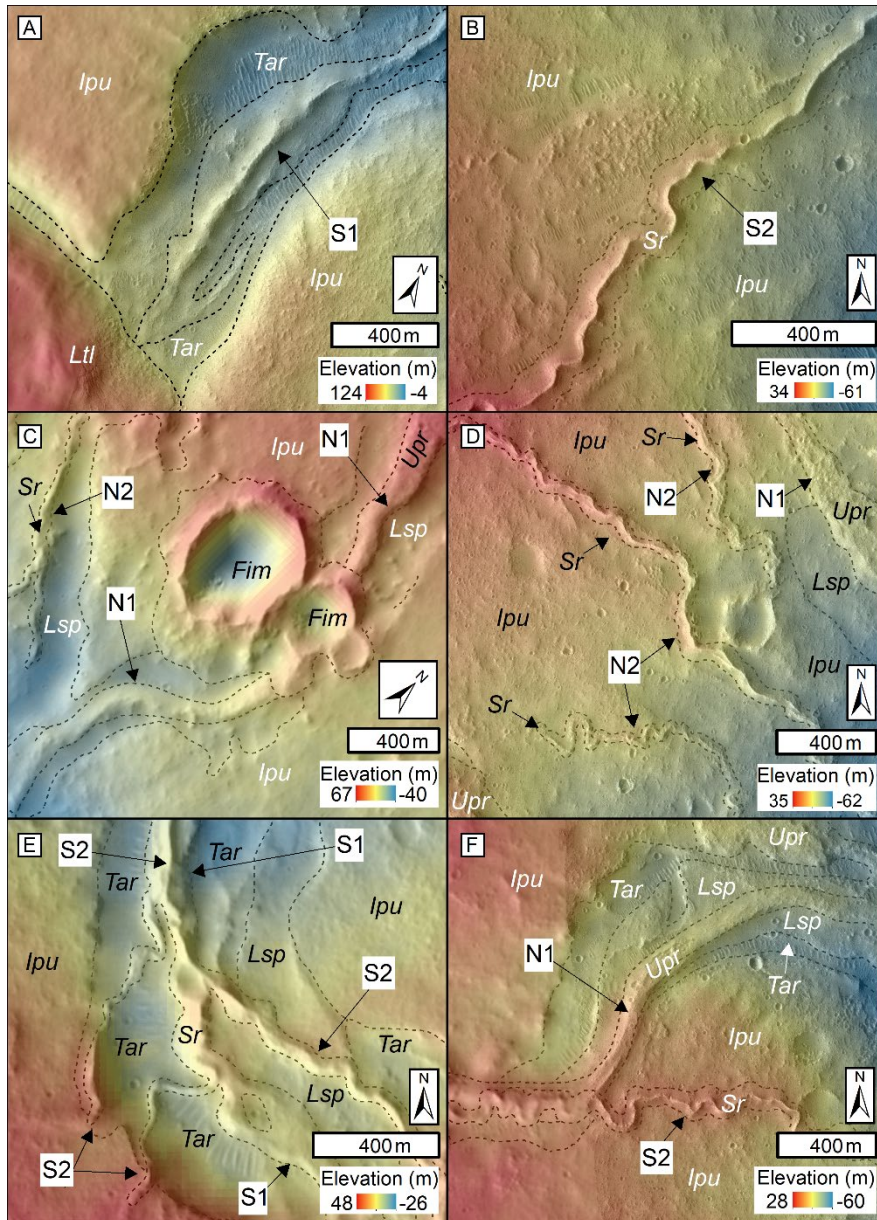


Figure 9. Sinuous ridges in Chukhung crater. (A) Sharp- to round-crested S1-type sinuous ridge within a valley on the southern floor. (B) Sharp-crested S2-type sinuous ridge crossing the intermediate plains on the southern floor. (C) Flat-topped to round-crested N1-type sinuous ridge within a valley on the northern floor. It is disrupted by fresh impact material. (D) Sharp-crested N2-type ridges crossing plains on the northern floor. (E) Dendritic network of sharp-crested S2-type ridges, which descend into a valley on the southern floor, then ascend the flanks of a flat-topped S1-type sinuous ridge occupying the valley floor, and continue down-valley atop its crest. (F) Sharp-crested S2-type ridge which superposes a flat-topped branch of an N1-type ridge on the south-western floor. The S2 ridge crosses onto a plateau east of the valley. Extents shown in Figure 7. Panels A–B and D–F are HiRISE images. Panel C and the western portion of panel F are CTX images. Panels A, C, E, and F are overlain by a 24 m/pixel CTX DEM. Panels B and D are overlain by a 1 m/pixel HiRISE DEM. See Figure 7 for unit abbreviations and Table S1 for data products.

247 floor: a stratigraphically-lower set of ridges (hereafter referred to as S1 ridges; Figure 9A),
248 and a stratigraphically-higher set of ridges (hereafter referred to as S2 ridges; Figure 9B). The
249 S1 ridges (n = 7) have typical lengths of ~1.4–4 km and typical sinuosities of ~1.1–1.2. The
250 S2 ridges (n = 9) have typical lengths of <1–4 km and typical sinuosities of ~1–1.6. Thus, the
251 S2 ridges are typically more sinuous than the S1 ridges.

252 Based on visual interpretation of crest morphologies from CTX and HiRISE images, the S1
253 ridges are predominantly sharp- to round-crested, but ~40% of S1 ridges also have flat-
254 topped sections. The S1 ridge with HiRISE DEM coverage (Figure 9A) has a typical height
255 of ~10–20 m and a typical width of ~150–300 m. The S2 ridges are sharp-crested. Those with
256 HiRISE DEM coverage (e.g., Figure 9B) are generally lower and narrower than S1 ridges,
257 having typical heights of ~7–10 m, and widths of ~100–150 m.

258 The S1 ridges occupy broad crater floor valleys which have widths of hundreds of meters and
259 depths of tens of meters (e.g., Figure 4F, Figure 8, and Figure 9A). The valleys extend across
260 the intermediate plains unit (*Ipu*; Figure 3, Figure 4L, and Figure 9A). The intermediate
261 plains unit is a low-relief, crater-concentric plains unit which dominates the crater floor
262 (Figure 3). The intermediate plains unit has a somewhat smooth appearance in southern
263 Chukhung crater and is comparatively rugged in the north (see Section 5.4). In contrast to the
264 S1 ridges, the S2 ridges do not conform to the axes of the crater floor valleys incised into the
265 intermediate plains unit. Four S2 ridges ascend the walls of those valleys and escape over the
266 lateral valley margins to cross onto the adjacent plateaus of the intermediate plains unit
267 (Figure 8B–C and Figure 9B). One S2 ridge crossing the intermediate plains is not hosted
268 within a crater floor valley. Five S2 ridges superpose S1 ridges, tracking along, or crossing
269 over, their crests (Figure 9E). In two locations, S2 ridge systems form quasi-dendritic
270 networks (Figure 3 and Figure 9E). In at least one location, an S1 ridge does not appear to
271 follow the central axis of its host valley, appearing to locally ascend and then descend the

272 valley wall; however, the ridge does not cross out of the valley at any point along its length
273 (Figure 8D).

274 The valleys within which many of the southern sinuous ridges are located are consistently
275 deeper than the heights of the ridges themselves. While seven crater floor valleys emerge
276 from beneath the LDA-terminal lobes or ridged plains units (Figure 8), nine similar (though
277 visibly shallower) valleys on the SE and E floor do not (Figure 3). Sinuous ridges are
278 uncommon, but not absent, within the valleys on the SE and E floor. The valley floors are
279 largely obscured by transverse aeolian ridges (TARs; Figure 4G; Balme et al., 2008). TARs
280 also occur on the floors of many small impact craters on the southern and eastern floor of
281 Chukhung crater (Figure 3 and Figure 4G). Where they coexist with sinuous ridges, TARs
282 superpose the flanks and crests of those ridges. The heads of the valleys on the SE and E
283 floor (and additionally the northern floor; See Section 5.4) commonly emerge from beneath
284 sinuous, finger-like extensions of a smooth plains unit (upper plains and ridges, *Upr*) which
285 appears to superpose the upslope margins of the intermediate plains unit (Figure 3, Figure
286 4K, Figure 5, and Figure 6). The surface texture of the upper plains and ridges unit is
287 similarly smooth and low-relief to the intermediate plains unit; however, the upper plains and
288 ridges unit forms positive-relief ridges extending from its downslope margins, whereas the
289 intermediate plains unit is valley-incised and does not appear to form positive relief features.

290 The downslope termini of the southern crater floor valleys are indistinct; they open out onto a
291 smooth plains unit (lower smooth plains, *Lsp*) which extends from low-relief contacts at the
292 lower margins of the intermediate plains unit, to the margins of the central pit (Figure 3 and
293 Figure 4M). The lower smooth plains have a more rugged surface texture than the
294 intermediate plains unit, and are primarily defined based on stratigraphic position below the
295 intermediate plains unit.

296 5.4 Northern Sinuous Ridges, Crater Floor Valleys, and Upper Plains

297 The northern portion of the floor of Chukhung crater also hosts assemblages of sinuous ridges
298 and valleys. As on the southern floor, valleys occur within the intermediate plains unit, and
299 expose lower smooth plains on their floors (Figure 7 and Figure 9C). However, in this portion
300 of the crater floor, the valley walls are less visually distinct (being more easily identifiable in
301 topographic profiles than in images), and the surrounding intermediate plains unit has a more
302 rugged and degraded texture than it has on the southern floor (Figure 10A and Figure 11).

303 Some of the northern crater floor valleys appear to be longitudinally discontinuous, though
304 the ejecta of numerous superposed impact craters obscures their relationships to downslope
305 valley segments (Figure 3 and Figure 4C). Unlike in the southern portion of the crater, the
306 valley floors are unobscured by TARs. Similarly to the valleys on the SE and E portions of
307 the crater floor, the northern crater floor valleys commonly emerge from beneath finger-like
308 extensions of the smooth upper plains and ridges unit (Figure 3, Figure 4K, Figure 10). On
309 the northern floor, many (though not all) of these finger-like features are continuous or
310 aligned with sinuous ridge systems (hereafter referred to as N1 ridges, $n = 18$, Figure 9C,
311 Figure 10, Figure 11), whose paths appear largely to conform to the axes of the valleys within
312 which they occur (Figure 9C). Approximately 20% of the sinuous ridges that extend from the
313 upper plains and ridges unit are not clearly associated with crater floor valleys (Figure 10B).

314 The N1 ridges have typical lengths of $\sim 1\text{--}7.5$ km and typical sinuosities of $\sim 1\text{--}1.2$. They
315 have more variable crest morphologies (including sharp-crested, round-crested, multi-crested,
316 and flat-topped) and more rugged surface textures than other sinuous ridges in Chukhung
317 crater (Figure 10 and Figure 11). They have variable topographic expression, ranging from
318 prominent ridges to low-relief features. In locations with HiRISE and CTX DEM coverage,
319 prominent ridge portions have typical heights of $\sim 5\text{--}20$ m and typical widths of ~ 150 m–
320 1.1 km.

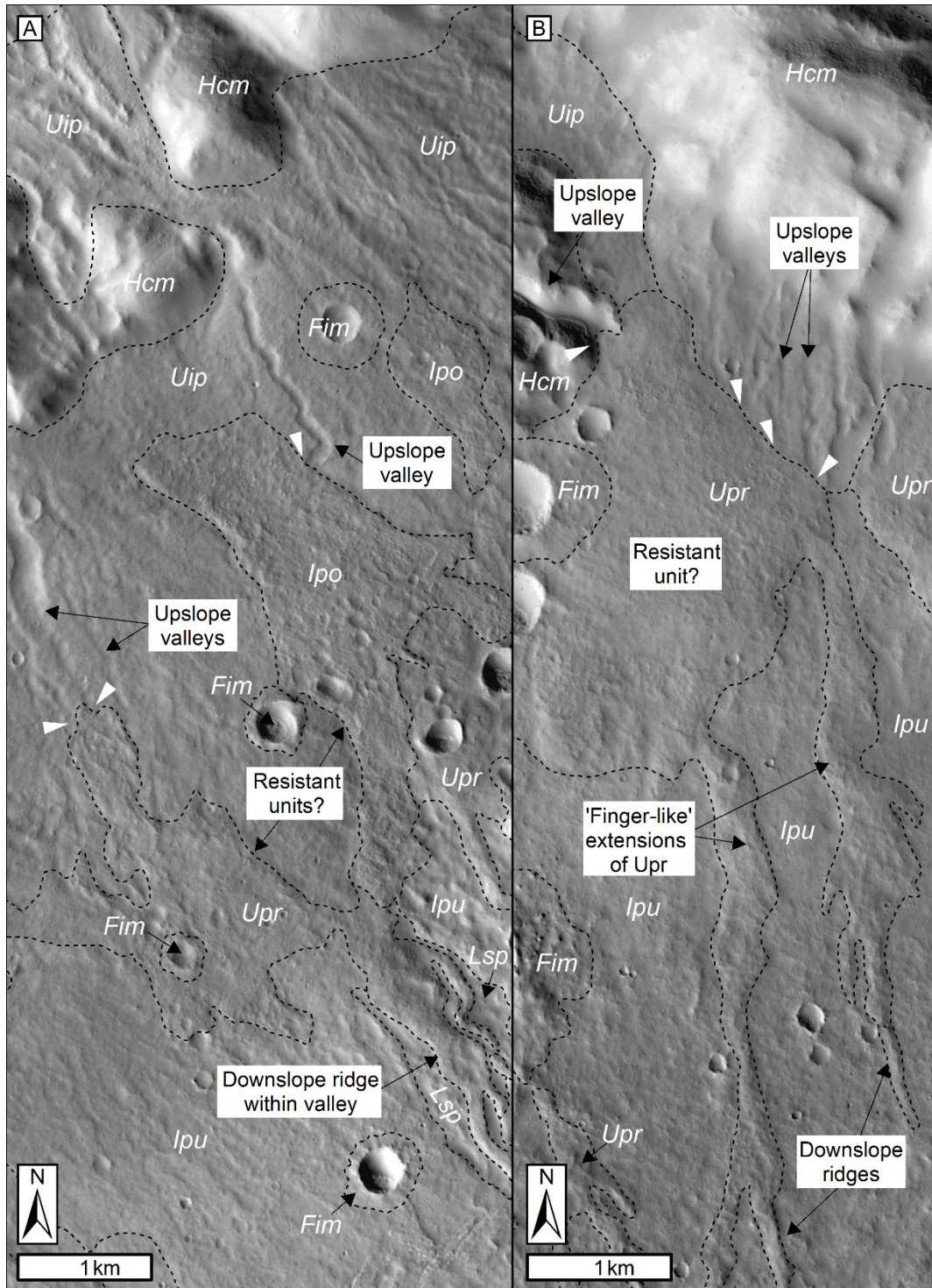


Figure 10. Relationships between upslope valleys and downslope sinuous ridges in the northern portion of Chukhung crater. (A) CTX image mosaic showing valleys within the Upper incised plains unit, which are superposed (white arrows) by the Upper plains and ridges (*Upr*) and Isolated pockmarked (*Ipo*) units downslope. Associated sinuous ridges extend downslope from the *Upr*. (B) CTX image mosaic showing crater wall valleys superposed by the *Upr* unit, and finger-like extensions from its downslope margins which transition into sinuous ridges. See Table S1 for data products.

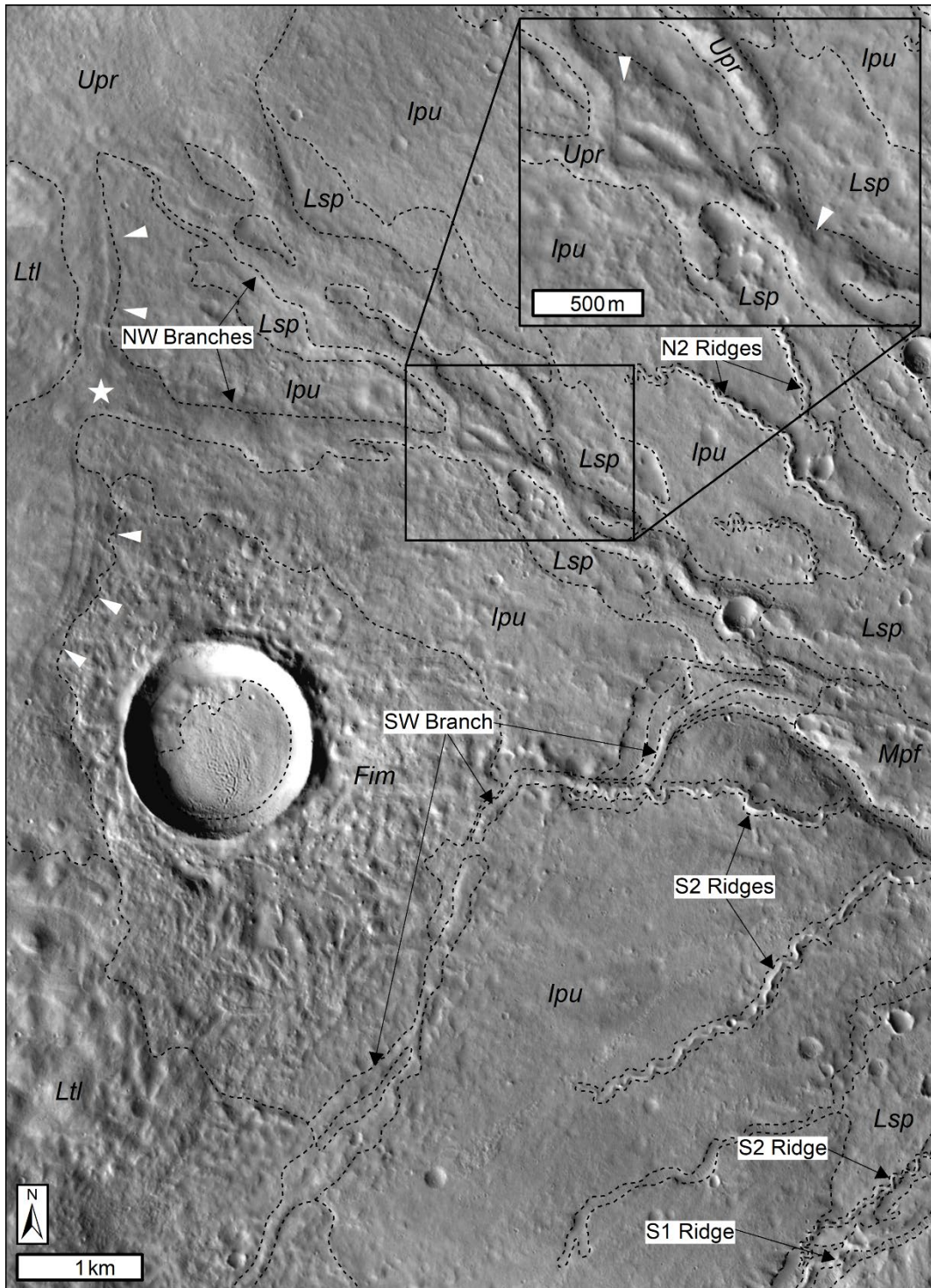


Figure 11. A prominent N1-type sinuous ridge on the NW floor of Chukhung crater. Key units are labelled (see Figure 3 for abbreviations). Plains-forming *Upr* materials appear to have internal layering (white arrows) where one of the NW branches emerges (white star). The NW branches might represent an anastomosing paleochannel network, but subtle elevation differences (white arrows in inset) may instead indicate migratory paleochannel systems at different stratigraphic levels. The SW branch emerges from the LDA-terminal lobe unit and is superposed by a S2-type ridge. CTX image mosaic (see Table S1 for data products).

323 A notable N1-type sinuous ridge network occurs on the WNW portion of the crater floor
324 (Figure 11). It is flat-topped, and has multiple branches that extend from the upper plains unit
325 to the NW. Another branch emerges from beneath the LDA-terminal lobe unit to the SW. The
326 SW branch may once have merged with the NW branch close to the margins of the crater's
327 central pit, but their relationship is obscured by a more recent impact crater (Figure 11). The
328 portion of the upper plains and ridges unit from which the NW branch emerges appears to be
329 layered (Figure 11, white arrows). Two of the NW branches appear to form an anabranching
330 network morphology, but close inspection suggests that the branches could be at different
331 stratigraphic levels (Figure 11, inset). The SW branch that emerges from the LDA-terminal
332 lobe is superposed by an S2 sinuous ridge, which trends west-to-east across the valley,
333 weaving along a ~600 m portion of the crest of the N1 ridge before extending eastward across
334 the adjacent intermediate plains unit.

335 Eleven sharp-crested ridge systems (hereafter referred to as N2 ridges) with very similar
336 morphologies and typical heights and widths to the S2 ridges (Section 5.3) also occur on the
337 northern portion of the floor of Chukhung crater (Figure 3 and Figure 9D). The N2 ridges
338 have typical sinuosities of 1–2.1. Several N2 ridges are not clearly associated with crater-
339 floor valleys; however, one example comprises two branches which extend along a valley
340 network emerging from beneath a finger-like extension of the upper plains and ridges unit (to
341 the NE of the box demarcating the extent of Figure 4A in Figure 3). Unlike the observed
342 relationships between S1 and S2 ridges, none of the N2 ridge systems appear to ascend valley
343 walls or cross the crests of N1 type ridges.

344 In many locations, the relationship between the northern sinuous ridges and deposits in the
345 central pit are obscured by small impact craters. However, where the N1 type sinuous ridges
346 can be traced to its margins, they appear to grade into central pit deposits.

347 5.5 Central Pit Units

348 As described above, the N–W margins of Chukhung crater’s central pit lack topographic
349 expression. Two of the major N1-type sinuous ridge networks that extend across the NW
350 portion of the crater floor appear to transition into a smooth unit which occupies the inner
351 margins of the central pit (marginal pit floor unit, *Mpf*; Figure 3, Figure 4I, and Figure 11).

352 The marginal pit floor unit extends unbroken from the northern margin of the central pit,
353 westward around its margins, to the base of the scarp at the SW margin of the central pit
354 (Figure 3). The surface of the marginal pit floor unit generally slopes towards the SE, but
355 well-preserved portions of its surface have flat tops (Figure 4I).

356 The eastern margins of the marginal pit floor unit have tens of meters of relief (Figure 4I and
357 Figure 6). Numerous outlying flat-topped and rounded mesas of marginal pit floor materials
358 occur beyond the eastern margins of the main deposit, their spatial density reducing towards
359 the center of the central pit (Figure 3 and Figure 4I). Similar mesas also occur around the NE,
360 W, and S margins of the central pit, and at the terminus of an S1 ridge (Figure 3).

361 The mesas of the marginal pit floor unit are surrounded by the unit that dominates the central
362 portion of the central pit: the central pit floor (*Cpf*) unit. The central pit floor is ~30 m lower
363 in elevation than the marginal pit floor unit and hosts a high density of variably-oriented
364 ridges in highly interconnected networks (Figure 4J). These ridges are morphologically
365 consistent with networks of interconnected TARs (e.g., Balme et al., 2008). The central pit
366 floor unit forms a ~20–30 m high scarp at its SE margin (Figure 4J), which suggests that the
367 unit is lithified. This scarp forms the wall of a ~400 m wide trench that separates the central
368 pit floor unit from the SE wall of the central pit. The floor of this trench is occupied by
369 numerous subparallel, trench-transverse TARs (Figure 4J).

370 5.6 Crater Wall Valleys and Upper Incised Plains

371 All portions of the wall of Chukhung crater that are not superposed by the LDA or highland
372 mantling units host sinuous, dendritic, kilometer-scale valley networks (Figure 3 and Figure
373 4O). These valley networks are considerably smaller than the 100 km-scale, Noachian-aged
374 valley networks in Mars' equatorial regions (e.g., Masursky et al., 1977; Hynek et al., 2010).
375 Many of the crater wall valleys incise smooth deposits (upper incised plains, *Uip*; Figure 3,
376 Figure 4N, and Figure 11) which occupy topographic lows in the crater wall (e.g. crater wall
377 terraces). In places, they extend several kilometers from the foot of the crater wall to the
378 upslope margins of the upper plains and ridges unit (Figure 10A). The downslope upper
379 plains and ridges unit overlies the upslope upper incised plains unit (Figure 5 and Figure 10).
380 In some locations, valleys within the upper incised plains are aligned with sinuous ridges and
381 valleys which extend from the downslope margins of the upper plains and ridges unit (Figure
382 3 and Figure 10). Isolated patches of rough, pockmarked material (Isolated pockmarked unit,
383 *Ipo*; Figure 4H) superpose both the upper incised plains and the upper plains and ridges units
384 (Figure 10A). The pockmarked texture comprises a mixture of small impact craters and
385 irregular-shaped pits.

386 5.7 Modeled Impact Crater Retention Ages

387 5.7.1 Estimation of the Age of Chukhung Crater

388 Chukhung crater is located within the early-Hesperian volcanic (eHv) unit, defined by
389 Tanaka et al. (2014b) as regionally-sourced flood lavas. Impact crater size-frequency
390 distributions return a best-fit model age of 3.59 Ga for the eHv unit (Tanaka et al., 2014a),
391 providing a maximum bounding age in the early Hesperian period for Chukhung crater.

392 Figure 12 shows the size-frequency distribution of impact craters superposed upon the ejecta
393 blanket of the SE rayed crater, which superposes the SE rim of Chukhung crater (Figure 2).

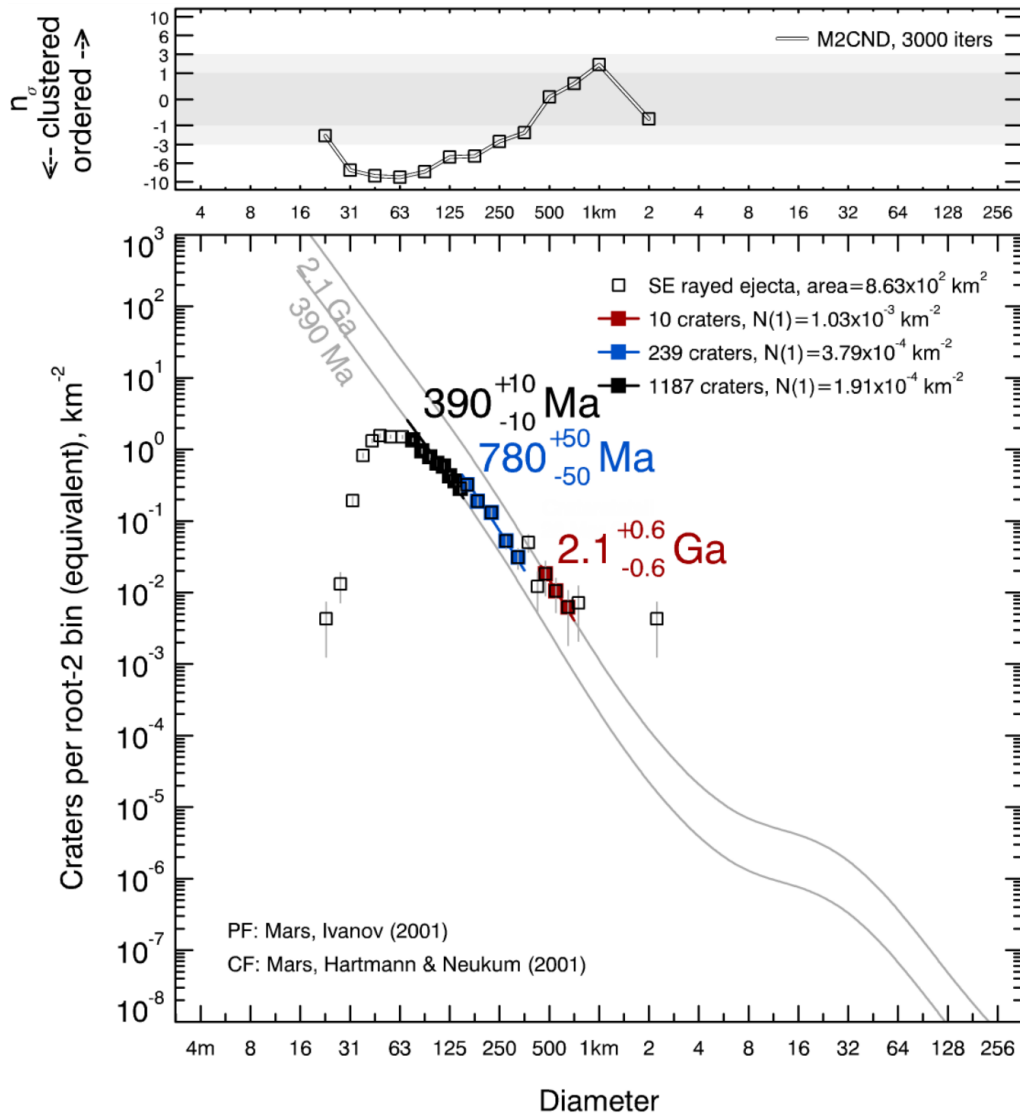


Figure 12. Impact crater size-frequency distribution for the ejecta blanket of the SE rayed crater. The lower axes are a log incremental plot (Hartmann, 2005) showing best-fit ages that follow three isochrones. Modeled ages are based upon the Ivanov (2001) production function and the Hartman and Neukum (2001) chronology function. The count area and locations of counted craters are shown in Figure 2. The roll-off for diameters <70 m represents the lower limit for reliable detection of impact craters. The upper axes show the results of spatial randomness analyses (Michael et al., 2012); the y-axis represents the number of standard deviations by which the M2CND (see text) of 3000 simulated impact crater populations deviates from the M2CND of the real impact crater population. Points within the grey region show that impact craters in the real population for a given diameter bin approximate a spatially random distribution. Points below the grey region show that impact craters in the real population for a given diameter bin are spatially clustered, possibly indicating the presence of secondary impact craters or the occurrence of heterogeneous resurfacing.

395 In total, we measured 1457 $D \geq 70$ m impact craters on the superposed impact ejecta
396 (8.63×10^2 km²; Figure 2), 1436 of which fall along isochrones defined by Hartmann and
397 Neukum (2001). $D(70\text{--}150$ m) impact craters ($n = 1187$) follow the 390 ± 10 Ma isochron,
398 $D(150\text{ m--}350$ m) impact craters ($n = 239$) follow the 780 ± 50 Ma isochron, and $D(450\text{ m--}$
399 700 m) impact craters ($n = 10$) follow the 2.1 ± 0.6 Ga isochron. We take a cautious approach
400 and use the maximum best-fit estimate of 2.1 ± 0.6 Ga derived from $D(450\text{ m--}700$ m) impact
401 craters as an estimate of the impact crater retention age of the superposed impact ejecta
402 blanket.

403 Spatial randomness analyses (Figure 12) of measured impact craters suggest that $D(450\text{ m--}$
404 700 m) craters, from which this age estimate was obtained, are spatially random, and
405 therefore that their size-frequency distribution is unlikely to have been strongly influenced by
406 resurfacing and/or secondary cratering processes. However, this best-fit age is derived from a
407 small sample of impact craters ($n = 10$) which, combined with the small count area (Warner
408 et al., 2015), introduces significant uncertainty into the 2.1 ± 0.6 Ga age estimate. Spatial
409 randomness analyses show clustering of the $D(70\text{ m--}350$ m) impact craters used to derive fits
410 to the 390 ± 10 Ma and 780 ± 50 Ma isochrons; thus, these fits may reflect resurfacing and/or
411 secondary impact cratering events during the middle Amazonian. Considering these new
412 analyses and the age of the eHv unit within which Chukhung crater is located (Tanaka et al.,
413 2014b), Chukhung crater probably formed $\sim 3.6\text{--}2.1$ Ga, between the early Hesperian and
414 early Amazonian.

415 5.7.2 Estimation of the Impact Crater Retention Age of VFFs in Chukhung Crater

416 We measured 309 impact craters across all LDAs within Chukhung crater (1.25×10^2 km²;
417 Figure 13), 133 of which fall along the Hartmann and Neukum (2001) isochrons. $D(50\text{--}90$ m)
418 impact craters ($n = 274$) follow the 84 ± 7 Ma isochron, while $D(150\text{--}300$ m) impact craters
419 ($n = 10$) follow the 330 ± 90 Ma isochron. The majority of $D(50\text{--}90$ m) impact craters on the

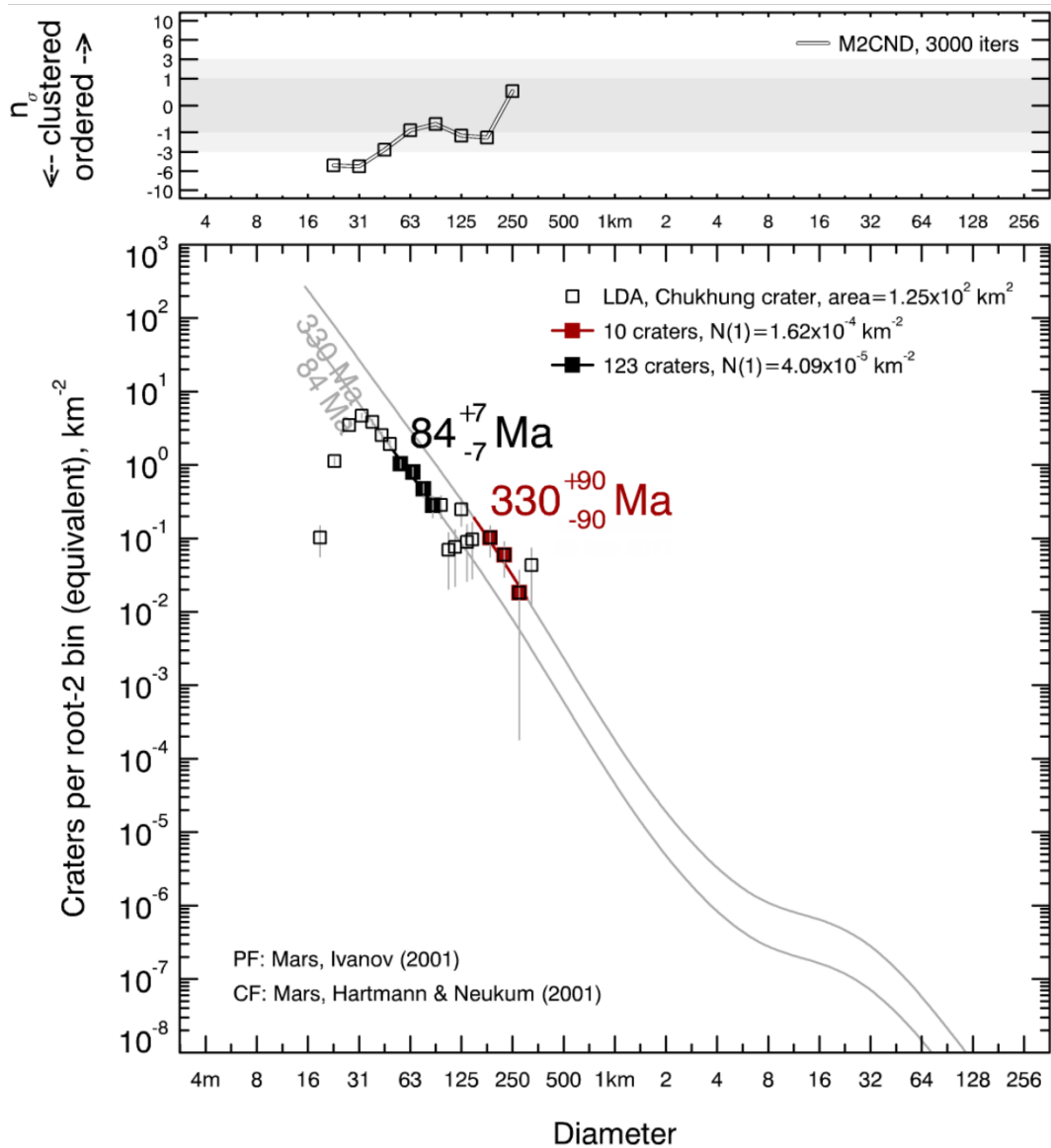


Figure 13. Impact crater size-frequency distribution for LDA in Chukhung crater. The lower axes are a log incremental plot (Hartmann, 2005) showing best-fit ages that follow two isochrones. Modeled ages are based upon the Ivanov (2001) production function and the Hartman and Neukum (2001) chronology function. The roll-off for diameters <50 m represents the lower limit for reliable detection of impact craters. The upper axes show the results of spatial randomness analyses (Michael et al., 2012); the y-axis represents the number of standard deviations by which the M2CND (see text) of 3000 simulated impact crater populations deviates from the M2CND of the real impact crater population. Points within the grey region show that impact craters in the real population for a given diameter bin approximate a spatially random distribution. Points below the grey region show that impact craters in the real population for a given diameter bin are spatially clustered, possibly indicating the presence of secondary impact craters or the occurrence of heterogeneous resurfacing.

421 LDAs have bowl-shaped morphologies, while $D(150\text{--}300\text{ m})$ impact craters have ‘ring-mold’
422 morphologies which have been attributed to modification of impact craters by deposition and
423 modification of mantling materials comprising ice-dust mixtures atop LDA surfaces (Baker
424 and Carter, 2019). Thus, the best-fit age of $84 \pm 7\text{ Ma}$ derived from $D(50\text{--}90\text{ m})$ impact
425 craters probably reflects the age of an episode of LDA resurfacing by a mantling deposit
426 during the late Amazonian. The best-fit age of $330 \pm 90\text{ Ma}$ derived from $D(150\text{--}300\text{ m})$
427 impact craters probably reflects the minimum age of the LDA in Chukhung crater, which
428 falls in the mid to late Amazonian.

429 However, the $D(50\text{--}200\text{ m})$ impact craters are not randomly spatially distributed. This could
430 make both modeled best-fit age estimates unreliable. Additionally, dependence upon impact
431 craters with $D < 100\text{ m}$ was unavoidable, potentially introducing a factor of ten uncertainty in
432 the $84 \pm 7\text{ Ma}$ fit (Hartmann, 2005). Unavoidably small count areas mean that the minimum
433 age estimate for LDAs ($330 \pm 90\text{ Ma}$) relies upon a small sample of impact craters ($n = 10$),
434 introducing additional uncertainty into this estimate (Warner et al., 2015). These
435 uncertainties are unavoidable and necessitate caution in interpretation of the ages of LDAs in
436 Chukhung crater. However, the key result, that the LDAs are young relative to the age of
437 Chukhung crater itself, is robust.

438 **6. Interpretations**

439 The floor of Chukhung crater has undergone significant post-impact modification. We now
440 discuss evidence that post-impact processes within Chukhung crater included subaerial
441 fluvial activity and more recent (possibly wet-based) glaciation. We first summarize the
442 ‘esker vs. inverted channel problem’ which affects interpretations of the origins of sinuous
443 ridge landforms on Mars (Section 6.1). With this context, we then discuss our hypothesis that
444 the landform assemblage comprising valleys and sinuous ridges in the northern portion of

445 Chukhung crater was formed by non-glacial (i.e., subaerial) fluvial processes, and argue that
446 the northern sinuous ridges are more likely to be inverted paleochannels than eskers (Section
447 6.2). We then discuss the hypothesis that landform assemblage comprising the LDA-terminal
448 lobes, ridged plains units, and sinuous ridges in southern Chukhung crater were formed by
449 glaciation, and that the southern sinuous ridges are eskers (Section 6.3). In Section 6.4 we
450 discuss the challenges for distinguishing between esker and inverted paleochannel origins for
451 sinuous ridges and, and in Section 6.5 explore the alternative hypotheses that all sinuous
452 ridges in Chukhung crater are inverted paleochannels, or that Chukhung crater hosts a
453 mixture of eskers and inverted paleochannels which cannot be divided on a north-south basis.
454 Finally, in Section 7, we discuss the paleoenvironmental implications of the landsystem in
455 Chukhung crater.

456 6.1 The ‘Esker vs. Inverted Paleochannel Problem’

457 Previous studies of sinuous ridges on Mars have commonly converged on a debate between
458 their origins as either eskers or inverted paleochannels (e.g., Howard, 1981; Tanaka and
459 Kolb, 2001; Banks et al., 2009; Burr et al., 2009; Williams et al., 2013; Kress and Head,
460 2015; Butcher et al., 2016). Similarities in the overarching process associated with the
461 formation of eskers and inverted paleochannels (i.e., the exhumation of sedimentary channel
462 fills from bounding material, whether that be ice or sediment) result in convergence of form
463 between eskers and inverted channels.

464 Confidence in a proposed formation mechanism for a given sinuous ridge on Mars can be
465 enhanced when that sinuous ridge is located within a wider landsystem that is geomorphically
466 consistent with the proposed mechanism (Pain et al., 2007; Burr et al., 2009; Gallagher and
467 Balme, 2015; Butcher et al., 2017). In the cases of the glacier-linked candidate eskers in
468 Phlegra Montes (Gallagher and Balme, 2015) and NW Tempe Terra (Butcher et al., 2017),
469 associations with VFFs and other landforms with possible glacial origins (e.g., moraines)

470 combined with a lack of corroborating contextual evidence for the alternative hypothesis that
471 they are inverted paleochannels, bolsters confidence in their origins as eskers.

472 An inverted paleochannel origin for sinuous ridges on Mars is often more easily diagnosed
473 than an esker origin. In many locations, topographic inversion not only exhumes individual
474 paleochannels, but paleochannel belts comprising inverted point and scroll bars, and/or cross-
475 cutting channel fills at different stratigraphic levels (Maizels, 1987; Williams et al., 2007;
476 Burr et al., 2009; Cardenas et al., 2018; Hayden et al., 2019; Balme et al., 2020). Such flow
477 migration features have not been identified in association with eskers on Earth; lateral
478 migration of a subglacial conduit typically (though not invariably) causes erosion of deposits
479 that trace former conduit locations. Thus, observations of migration features in association
480 with a sinuous ridge on Mars can improve confidence in an inverted paleochannel origin.

481 The ‘esker vs. inverted paleochannel problem’ is most acute in the case of sinuous ridges that
482 are not associated with corroborating evidence for channel migration. Such features may be
483 absent in the vicinity of an inverted paleochannel because of preferential induration and/or
484 preservation of a single channel, or a lack of migration of the original channel (e.g., Williams
485 et al., 2013). Previous workers have appealed to several other geomorphic characteristics to
486 favor either inverted paleochannel or an esker origins for sinuous ridges on Mars, including:
487 (1) ridge crest morphology, (2) relationship of the ridge with the path of steepest topographic
488 descent, (3) 3D ridge morphometry, and (4) ridge sinuosity. However, as we will discuss,
489 there are unresolved caveats for the use of these criteria for distinguishing between eskers and
490 inverted paleochannels on Mars.

491 6.2 Northern Chukhung Crater: Fluvial Activity and the Inverted

492 Paleochannel Hypothesis

493 Central pit craters on Mars commonly host valley networks and other landforms of putative
494 fluvial origin (e.g., alluvial fans and paleolake deposits) which have been attributed to
495 localized precipitation and/or snowmelt during the Hesperian or Amazonian (Peel and
496 Fassett, 2013). These valley networks commonly occur on the floors of central pit craters and
497 on the crater walls. In some central pit craters, crater wall valleys are continuous with crater
498 floor valleys. Peel and Fassett (2013) identified Chukhung crater as hosting such valley
499 networks, and noted that several of those valleys are topographically inverted.

500 Our observations of the northern portion of Chukhung crater are in agreement with those of
501 Peel and Fassett (2013). The ubiquitous occurrence of dendritic valley networks on the
502 unglaciated portions of the walls of Chukhung crater (Figure 3), and commonly originating
503 near to the crater rim crest, is consistent with subaerial fluvial drainage from a distributed
504 source, such as rain or snowmelt (Peel and Fassett, 2013). We interpret the upper incised
505 plains unit as fluvial deposits based on the continuity between valleys within this unit and
506 valleys on the crater walls, and the tendency of the unit to occupy topographic lows. The
507 alignment of several valleys within the upper incised plains with finger-like extensions from
508 the downslope margins of the upper plains and ridges unit (Figure 10) leads us to propose that
509 the upper plains and ridges unit comprises resistant (e.g., indurated and/or coarse-grained)
510 materials. These formed within the upper layer(s) of, or atop, the upper incised plains, and
511 within the crater floor valleys downslope, enabling topographic inversion of channels or
512 channel belts downslope, and the formation of inverted paleochannels.

513 Combined with the evidence discussed above, the occurrence of many N1-type ridges within
514 negative-relief crater-floor valleys mean that they probably represent inverted valley-interior

515 channels or channel belts (e.g., Cardenas et al., 2018; Davis et al., 2019), and that they were
516 exhumed by removal of more susceptible materials on the valley floors. Sinuous ridges that
517 appear to cross one-another, possibly at different stratigraphic levels, along the major N1-
518 type sinuous ridge network on the NW floor of Chukhung crater (Figure 11) suggest that the
519 ridges might be remnants of migratory channel systems (e.g., Williams et al., 2007). The
520 rugged texture of the intermediate plains unit in the northern portion of Chukhung crater, and
521 the visual subtlety of the valley walls, suggests that significant regional deflation may have
522 accompanied channel exhumation, but that this deflation was insufficient to completely erase
523 the original host valleys.

524 The isolated pockmarked unit shows similar relationships with upslope valleys and
525 downslope sinuous ridges to that exhibited by the upper plains and ridges unit (Figure 4H).
526 However, the limited, discontinuous extent of the isolated pockmarked unit leads us to
527 suggest that it did not have a significant influence on broad-scale topographic inversion of the
528 crater floor. Its pockmarked texture, patchy distribution, and lack of clear source within the
529 crater suggests that it could be an airfall deposit. However, its limited extent makes
530 constraining its origins difficult, so we do not speculate further.

531 Peel and Fassett (2013) noted common relationships between valley networks and deposits
532 within central pit craters on Mars, which they interpreted as fluvial or lacustrine in origin.
533 Given that some of the northern sinuous ridges grade into the marginal pit floor unit (e.g.,
534 Figure 11), we propose that the marginal pit floor unit could represent erosional remnants of
535 lithified fluvial or lacustrine deposits which were transported to Chukhung crater's central pit
536 by fluvial valley networks. The materials could have been deposited in a paleolake, or they
537 could be highly-eroded remnants of alluvial fan deposits, which may be more consistent with
538 the general slope of the unit towards the SE (Figure 6). The marginal pit unit probably
539 covered the floor of the central pit more extensively in the past because: (a) there are several

540 isolated mesas of marginal pit floor materials throughout the central pit, including around its
541 N and E margins (Figure 3); and (b) there is evidence for significant aeolian modification
542 (and possibly removal) of valley-distal materials on the central pit floor (in the central pit
543 floor unit; Figure 4J). We propose that aeolian-driven retreat of the marginal pit floor unit has
544 exposed the central pit floor unit. Preferential preservation of the marginal pit floor unit close
545 to the termini of the northern sinuous ridges (Figure 3 and Figure 6) is consistent with the
546 deposition of coarse-grained sediments proximal to the contributory valley networks.
547 Deposition of susceptible, fine-grained sediments in valley-distal positions would explain
548 preferential retreat of the marginal pit floor unit from the central to eastern portions of the
549 central pit. The ~30 m deep trench along the SE margin of the central pit floor (Figure 4J)
550 unit suggests that post-impact deposits of at least 30 m thickness remain in the central pit
551 floor unit.

552 Landform relationships on the northern wall and floor of Chukhung crater (including
553 associations of the N1-type sinuous ridges with upslope valleys and possible resistant
554 materials within the upper plains and ridges unit, and evidence for migration of ridge-forming
555 flows) are most consistent with the origins of the N1 ridges as inverted paleochannels.
556 Combining this with the lack of evidence for past or present glaciation or ice-rich mantling of
557 the northern wall or floor of Chukhung crater, it is considerably more likely that the N1
558 ridges are inverted paleochannels than that they are eskers. The relationships between sinuous
559 ridges, crater wall valleys, and possible resistant materials in the upper plains and ridges unit,
560 and the migratory characteristics observed for N1-type ridges, are not observed for N2-type
561 ridges. Therefore, some uncertainty remains over the origins of the N2 ridges; however, the
562 alignment of some N2 ridges with the downslope ends of N1 ridges, and the lack of evidence
563 for past or present glaciation on the northern floor of Chukhung crater suggests that they are
564 more likely to be inverted paleochannels than eskers.

565 6.3 Southern Chukhung Crater: Glaciation and the Esker Hypothesis

566 The southern portion of Chukhung crater is presently glaciated. The convex-up topographic
567 profiles of many portions of the LDAs suggests they may retain substantial cores of debris-
568 covered ice. However, concave topographic profiles in some portions, and the highly tortuous
569 LDA termini (as opposed to smooth, lobate termini) imply that the LDAs have probably
570 undergone significant downwasting and retreat since they reached their maximum volume
571 and extent.

572 We interpret the LDA-terminal lobes that bound LDAs on the southern floor as moraines
573 formed by downwasting of the LDAs following stagnation of the glacier termini. Hummocks
574 and arcuate ridges within the LDA-terminal lobes are morphologically similar to hummocky
575 moraines on Earth, which commonly contain substantial ice cores (e.g., Hambrey et al., 1997;
576 Krüger and Kjær, 2000). Thus, the LDA-terminal lobes could contain substantial extant ice
577 cores mantled by debris derived from supraglacial dust and/or debris cover. We cannot,
578 however, rule out that some fraction of lithic material in the LDA-terminal lobes was derived
579 from subglacial erosion. In their global survey of martian impact craters using 100–
580 233 m/pixel Thermal Emission Imaging System daytime infrared images, Robbins and Hynek
581 (2012) categorized these features as crater wall slump deposits formed by mass wasting of the
582 crater wall or rim. The higher-resolution CTX and HiRISE images and topographic data
583 analyzed in the present study support a moraine interpretation because: (a) the lobes are
584 consistently spatially associated with LDAs, and (b) we find insufficient evidence for a
585 source region (e.g., consistently spatially-associated crater wall alcoves, depressions in the
586 elevation of the crater rim, or north-south asymmetry of the crater walls) for a slump event of
587 the magnitude implied by the extensive and voluminous nature of the LDA-terminal lobes.
588 Our ice-cored moraine interpretation does not require that the full volume of the LDA-
589 terminal lobes was derived from subglacial erosion of the crater walls/floor. However, we

590 note that the crater wall above the present-day LDA surfaces has a ‘planed-off’ appearance,
591 which differs from the prominent valley-interfluvial morphology of the northern crater wall,
592 and could be related to glacial erosion (Figure S2). An alternative explanation for the
593 formation of the LDA terminal lobes is that they are impact ejecta deposits from the SE rayed
594 crater, and we discuss the implications of this hypothesis further below. However, their
595 orientations (particularly of the LDA-terminal lobes in SW and W Chukhung) seem
596 inconsistent with having been sourced from the SE rayed crater. Additionally, their
597 morphologies are different in character to other portions of the ejecta blanket of the SE rayed
598 crater, although it is conceivable that this could result from interaction of impact ejecta with
599 the steep rim topography of Chukhung crater.

600 The ridged plains unit lacks the decametre-scale undulations observed within the LDA-
601 terminal lobe unit, but its spatial association with other glacial units suggests that it could
602 be a ground moraine deposited by the LDAs. However, the ridged plains unit hosts numerous
603 subparallel lineae that align with rays within the ejecta of the SE rayed impact crater located
604 ~10 km SE of Chukhung crater. The northern margin of the ridged plains unit is ~24 km from
605 the NW rim of the SE rayed crater, which is comparable to the ~25 km distance between its
606 SE rim and the SE margins of its distal ejecta blanket. Thus, the lineations within the ridged
607 plains unit could comprise distal ejecta from that impact (see Section 5.2). The absence of
608 evidence for ejecta or similar lineae on nearby LDAs or LDA-terminal lobes suggests that the
609 ejecta was emplaced prior to the most recent glaciation. Alternatively, the ridged plains unit
610 could have been emplaced as an isolated patch of impact ejecta atop the LDA-terminal lobes,
611 driving deflation of ice within the underlying deposits and explaining the atypical low-relief
612 transition between the LDA-terminal lobe and sinuous ridges via the ridged plains unit in this
613 location. However, the lineae in distal ejecta SE of the parent impact crater (Figure 14C) are
614 significantly more pristine than the lineae in the ridged plains unit (Figure 14B) within

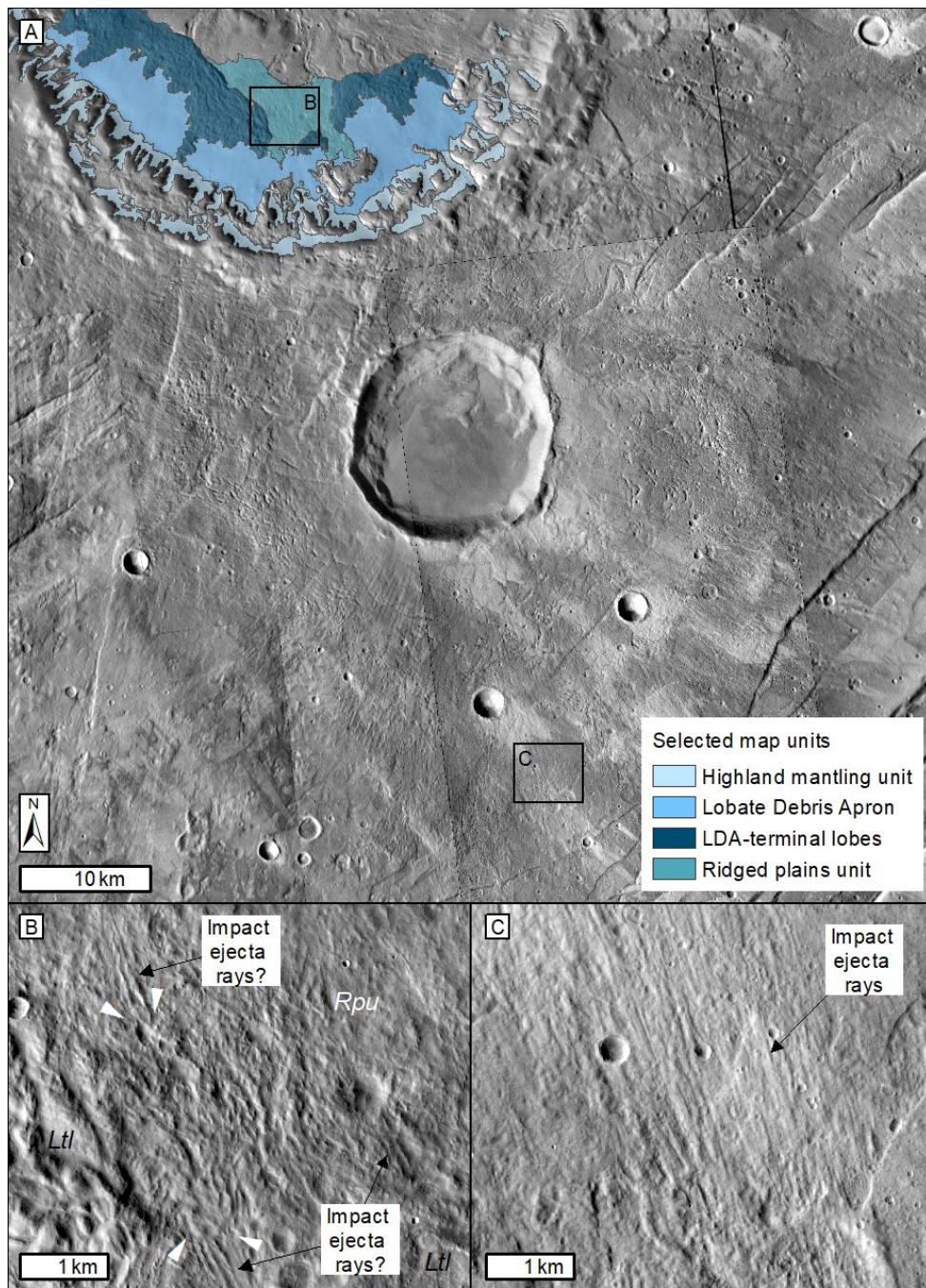


Figure 14. Evidence for glacial modification of rayed impact ejecta in Chukhung crater. (A) CTX image mosaic (see Table S1) showing the rayed impact crater SE of, and inferred glacial and glacial units within, Chukhung crater, and the extents of panels B and C. (B) Possible ejecta from the SE rayed impact crater within the Ridged plains unit (Rpu), which appears to have been overprinted (white arrows) by materials that grade into the LDA terminal lobes (Ltl). (C) Rayed ejecta on the opposite (SE) side of the impact ejecta blanket, but at a similar distance from the parent crater rim to panel B. The ejecta rays here are relatively morphologically pristine. This suggests that rayed ejecta within Chukhung crater has been modified by processes that haven't occurred elsewhere on the ejecta blanket (i.e., glaciation).

616 Chukhung crater, suggesting that the lineae within Chukhung crater have been modified, for
617 example by glacial overprinting. In some locations within the ridged plains unit in Chukhung
618 crater, the lineae are superposed by materials with hummocky morphologies that are similar
619 to (but have lower relief than) those within the LDA-terminal lobes. Thus, the ridged plains
620 unit may comprise distal rayed ejecta from the SE rayed crater, but this impact ejecta may
621 have been modified and partially buried by moraines during subsequent glaciation. The
622 hummocky topography of the LDA-terminal ridge and ridged plains units could have resulted
623 from either sublimation or melting of dead ice. However, we find no evidence of meltwater
624 drainage from the LDA-terminal lobe complex, and therefore argue that sublimation was the
625 dominant or sole contributor to ice loss from this unit.

626 Given the spatial association of the southern (S1 and S2) sinuous ridges with LDAs (i.e.
627 putative debris-covered glaciers) and possible glacial deposits in the LDA-terminal lobe
628 and ridged plains units (Figure 8), we explore their possible origins as eskers formed during
629 one or more phase(s) of wet-based glaciation in southern Chukhung crater.

630 Most notable among the esker-like characteristics of the southern sinuous ridges, aside from
631 their associations with glacial deposits, are: (a) their ascent of valley walls and
632 topographic divides (e.g., Figure 8B–D); (b) similarities between their crest morphologies
633 and those of eskers on Earth (e.g., Shreve, 1985; Perkins et al., 2016), being predominantly
634 sharp-crested, but also having round-crested and flat-topped portions (e.g., Figure 8B–D and
635 Figure 9A–B); and (c) similarities between their typical morphometries and those of martian
636 sinuous ridges for which we are relatively confident of esker origins (Gallagher and Balme,
637 2015; Butcher et al., 2017; Butcher, 2019; Butcher et al., 2020).

638 Eskers deposited by pressurized meltwater in ice-confined subglacial conduits commonly
639 ascend topographic undulations due to modification of the direction of steepest hydraulic

640 potential gradient by the overlying ice (e.g., Shreve, 1972, 1985). Thus, subglacial formation
641 as eskers could explain why the S2 sinuous ridges in Chukhung crater do not conform to the
642 axes of the crater floor valleys, and in some cases ascend valley walls and cross onto adjacent
643 plains. In this regard, they are strikingly esker-like (Figure 15).

644 Qualitatively, the crest morphologies of both the S1 and S2 ridges are very similar to those of
645 eskers on Earth (e.g., Figure 15), being dominated by prominent sharp crests. Preliminary
646 measurements suggest that their typical geometries (Section 5.3) are similar to mid-latitude
647 VFF-linked sinuous ridges in Phlegra Montes (Gallagher and Balme, 2015; Butcher, 2019)
648 and NW Tempe Terra (Butcher et al., 2017; Butcher, 2019), for which we are confident of
649 esker origins.

650 The S1 type sinuous ridges emerge from beneath the LDA terminal lobe and ridged plains
651 units, which we have interpreted as moraines. Thus, if the southern sinuous ridges are eskers,
652 they pre-date the moraine-forming episode, and the glaciers previously extended beyond the
653 LDA-terminal ridges, up to ~15 km across the crater floor, towards the margins of the central
654 pit. Under the esker hypothesis, one or more episodes of basal melting and esker formation
655 accompanied, or were followed by, glacier retreat. Subsequent glacier stagnation and
656 downwasting of the LDA termini, either by sublimation or melting of ice, could explain the
657 formation of the moraine deposits which superpose the heads of the sinuous ridges (LDA-
658 terminal lobes and ridged plains units). The absence of moraine ridges at the termini of the
659 sinuous ridges does not pose a significant challenge for the esker hypothesis. Eskers on Earth
660 are commonly found without associated moraines (e.g., Aylsworth and Shilts, 1989), for
661 example due to: transience of wet-based conditions; short-lived glacial advance followed by
662 continuous retreat; and/or low rates of basal sliding (and hence erosion and sediment
663 production) associated with efficient evacuation of meltwater through esker-forming
664 meltwater conduits.

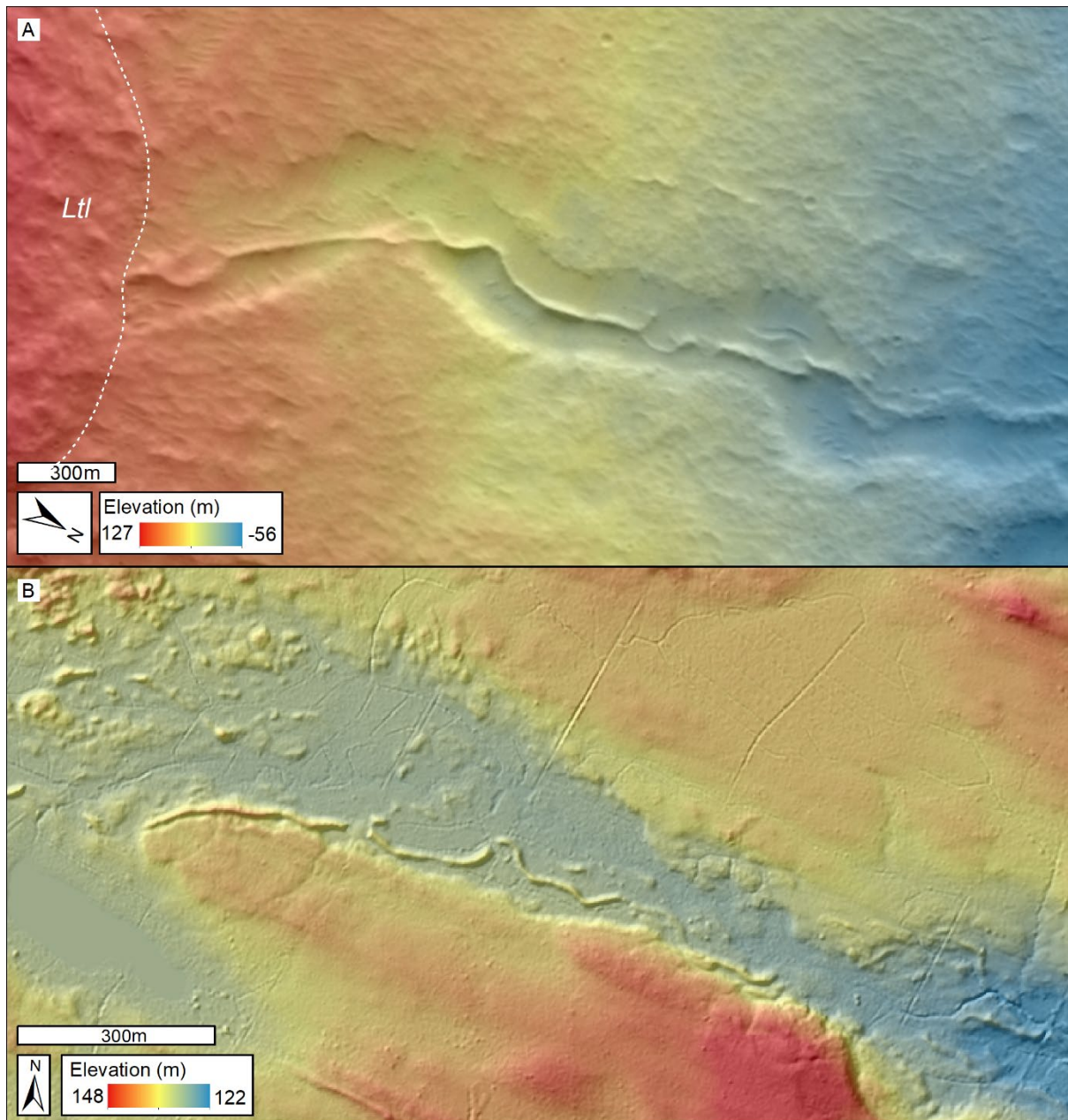


Figure 15. Similarities in morphology and associations with host valleys between sinuous ridges in Chukhung crater, Mars, and eskers in Finland, Earth. (A) 6 m/pixel CTX image mosaic overlain with 24 m/pixel CTX stereo-pair-derived DEM of an S1-type sinuous ridge which emerges from the LDA-terminal ridge unit and appears to ascend the wall of the crater-floor valley it occupies. Extent shown in Figure 7. (B) Shaded relief map overlain with 2 m/pixel LiDAR DEM of an esker in southern Finland, Earth (panel centered on 24.117°E, 60.871°N). The esker occupies a broader meltwater valley, and does not adhere to the topography of the valley axis. The similarities in morphology and topographic setting between the ridges in panels A and B are striking. Paleoflow in both panels was from left to right. See Table S1 for list of data products.

666 An esker interpretation of the southern sinuous ridges is dependent upon the interpretation of
667 the LDA-terminal lobes as moraines. If the LDA-terminal lobes are impact ejecta or crater
668 wall-slump deposits (Robbins and Hynek, 2012), these units instead represent a temporal
669 discontinuity between formation of the sinuous ridges that they superpose, and the formation
670 of the LDA. In this case, units underlying the LDA-terminal lobes, including the sinuous
671 ridges, formed before the SE impact crater ~ 2.1 Ga. If the ridged plains unit comprises pre-
672 glacial impact ejecta over which glaciers did not subsequently advance, this would also
673 represent a temporal discontinuity between the LDA upslope and the sinuous ridges
674 downslope. Alternatively, if the ridged plains unit is a patch of outlying impact ejecta
675 emplaced after formation of the LDA-terminal lobes, then the LDA, LDA-terminal lobes, and
676 sinuous ridges could have formed within the same glacial event. If this scenario is correct,
677 this would suggest that our impact crater size-frequency analyses significantly underestimate
678 the age of the extant glaciers in Chukhung crater, and that the glaciers advanced before the
679 formation of the SE impact crater ~ 2.1 Ga (i.e., during or prior to the early Amazonian).
680 However, we consider this scenario to be unlikely based on the apparent superposition of
681 hummocky materials (similar to those within the adjacent LDA-terminal lobes) atop ejecta
682 lineae within the ridged plains unit.

683 Eskers on Earth are commonly associated with tunnel valleys, which form under erosive
684 regimes of subglacial drainage (e.g., Kehew et al., 2012). If the southern sinuous ridges are
685 eskers, the crater floor valleys with which they are associated could be interpreted as tunnel
686 valleys. However, similar crater floor valleys occur around all portions of Chukhung crater,
687 including in portions with no additional evidence of past or present glaciation. Similar valleys
688 are also common within central pit craters elsewhere on Mars, in which there is often no
689 associated evidence of past or present glaciation (Peel and Fassett, 2013). We find little
690 additional evidence (other than the association of some of the valleys with esker-like sinuous

691 ridges) to challenge the hypothesis of Peel and Fassett (2013) that the crater floor valleys
692 within Chukhung crater are pre-glacial subaerial fluvial valleys of Hesperian or Amazonian
693 age. However, if glaciers within Chukhung crater did subsequently produce meltwater, this
694 meltwater is likely to have exploited pre-existing valleys. Under the esker hypothesis, this
695 would explain why the southern sinuous ridges generally occupy the valleys; deviations in
696 the paths of the sinuous ridges from the valley axes, and the crossing of S2 ridges out of the
697 valleys, can be explained by localized modification of hydraulic gradients by the overlying
698 ice.

699 6.4 Challenges for the Esker Hypothesis

700 Chukhung crater demonstrates the challenges for interpreting the origins of sinuous ridges on
701 Mars in locations where contextual landsystems consistent with paleochannel inversion (i.e.,
702 fluvial valleys, and evidence for channel migration and subsequent landscape deflation) and
703 esker formation (i.e., extant glaciers and glacial deposits) coexist in close proximity.

704 The highland mantling, LDA, LDA-terminal lobe, and ridged plains units obscure
705 topographic lows in the southern crater wall, and the intermediate-to-upper elevations of the
706 southern crater floor. It is in these portions of northern Chukhung crater that the landform
707 associations providing strongest evidence for inverted paleochannel origins of the N1 sinuous
708 ridges (i.e., associations with crater wall valley networks and a possible resistant unit) are
709 observed (Figure 10). The near-ubiquitous distribution of valley networks on all portions of
710 the crater wall where highland mantling materials are absent suggests that the highland
711 mantling unit could obscure similar valley networks on the southern crater wall. Thus, it is
712 possible that, despite their associations with glacial deposits, the southern sinuous ridges in
713 Chukhung crater are also inverted paleochannels that pre-date glaciation. The SW branch of
714 the major N1-type sinuous ridge network on the NW portion of the crater floor emerges from

715 beneath the LDA-terminal lobe on the SW floor, demonstrating that the LDAs do obscure
716 ridges interpreted as inverted paleochannels in some locations.

717 In such circumstances where contextual landsystems are consistent with both esker and
718 inverted paleochannel origins for sinuous ridges on Mars, it is necessary to appeal to
719 properties of the ridges themselves to explore possible formation mechanisms. In the sections
720 that follow, we consider the key esker-like characteristics of the southern sinuous ridges in
721 more detail, and highlight the caveats of using some of these characteristics to definitively
722 exclude an inverted paleochannel origin.

723 6.4.1 Ridge Crest Morphology

724 As discussed in Section 5.3, the southern sinuous ridges in Chukhung crater have similar
725 (predominantly sharp-crested) morphologies to eskers on Earth. Arguments that favor esker
726 or inverted paleochannel origins for sinuous ridges based on their typical crest morphologies
727 (e.g., Kargel and Strom, 1992; Pain et al., 2007; Burr et al., 2009) are rooted in an informal
728 understanding that inverted paleochannels are typically flat-topped, and eskers are more often
729 characterized by one or more sharp or rounded medial crests.

730 However, on Earth, neither morphology is unique to inverted paleochannels or eskers (Figure
731 16). Although inverted paleochannels are predominantly flat-topped (Figure 16A and C; Pain
732 et al., 2007; Williams et al., 2007), they can have crest morphologies (Williams et al., 2013;
733 Chuang and Williams, 2018) that are similar to eskers (Shreve, 1985; Perkins et al., 2016),
734 including: round-crested, sharp-crested, and multi-crested sections, and sections that retain
735 negative-relief troughs (Maizels, 1987; Pain and Oilier, 1995; Williams et al., 2007).

736 Additionally, the crest morphologies of inverted paleochannels can evolve over time. The
737 flat-topped morphology shown in transect C–C' in Figure 16A and Figure 16C results from
738 the preservation of resistant caprock at the crest of an inverted paleochannel on Earth. In the

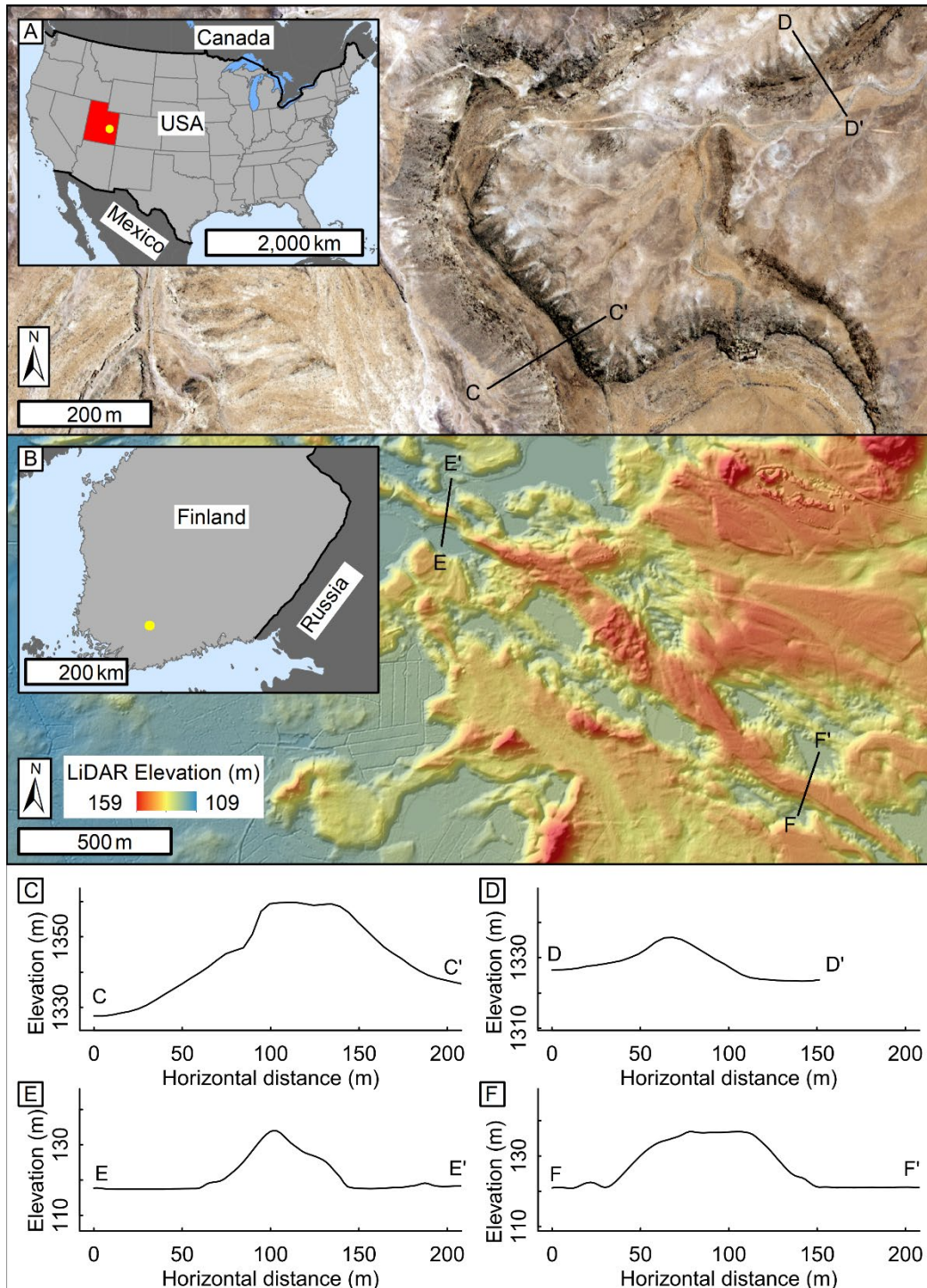


Figure 16. Morphological similarities between eskers and inverted paleochannels on Earth. (A) Aerial orthophotograph (illumination from left) of inverted paleochannels in Utah (location 110.273°W, 38.878°N shown by yellow point in inset map) showing locations of cross-sectional topographic profiles (at 5 m/pixel resolution) C–C' (panel C, a flat-topped portion), and D–D' (panel D, a sharp- to round-crested portion). (B) 2 m/pixel LiDAR DEM of an esker in SW Finland (location 23.992°E, 60.746°N shown by yellow point in inset map) showing locations of cross-sectional topographic profiles E–E' (panel E, a sharp-crested portion), and F–F' (panel F, a flat-topped portion). See Table S1 for data products.

740 location of transect D–D' (Figure 16A and Figure 16D), however, removal of the caprock has
741 exposed more susceptible underlying materials and subsequent erosion has driven a transition
742 to a sharp-to-round-crested morphology (See also Figure 10 in Burr et al., 2009). Some
743 eskers on Earth also have flat-topped morphologies (Figure 16B and Figure 16F; Kargel and
744 Strom, 1992; Perkins et al., 2016). Flat-topped eskers are thought to form by deposition
745 within subaerial ice-walled channels, or within subglacial conduits at atmospheric pressure
746 (i.e., under non-channel-full conditions; e.g., Burke et al., 2012; Perkins et al., 2016).
747 Therefore, distinguishing between eskers and inverted paleochannels on Mars based on their
748 crest morphologies alone represents an oversimplification. Indeed, ~40% of the S1 ridges in
749 southern Chukhung crater transition between sharp-crested and flat-topped morphologies at
750 one or more point(s) along their lengths. The predominance of sharp-crested morphologies
751 along the southern sinuous ridges in Chukhung crater, while esker-like, is therefore not
752 uniquely indicative of esker origins, despite striking visual similarities to typical eskers on
753 Earth.

754 Additionally, N2-type ridges on the northern floor of Chukhung crater (Figure 9D) have very
755 similar sharp-crested morphologies and scales to many S2-type ridges on the southern floor
756 (Figure 9B). Some of these N2-type ridges originate close to the downslope ends of N1-type
757 ridges and are aligned with them. There is no evidence for either past or present glaciation of
758 the northern portion of Chukhung crater. Thus, the morphological similarity between N2- and
759 S2-type ridges could be problematic for the esker hypothesis.

760 6.4.2 Ascent of Bedslopes

761 One of the most commonly-invoked arguments to support esker origins for sinuous ridges on
762 Mars is ascent of bedslopes by those ridges (Head, 2000a, 2000b; Head and Hallet, 2001a,
763 2001b; Banks et al., 2009; Burr et al., 2009; Butcher et al., 2016, 2017), as we observe for the
764 southern sinuous ridges in Chukhung crater. Under hydraulic pressure within confined

765 subglacial conduits, subglacial meltwater follows the hydraulic gradient, which is controlled
766 primarily by ice surface slope, rather than bed topography (Shreve, 1972, 1985). Thus, esker
767 paths commonly deviate from the steepest topographic slope or even ascend topography. This
768 contrasts markedly with subaerial rivers, whose paths invariably follow the steepest
769 topographic gradient. As a result, ascent of bedslopes (such as we observe for the southern
770 ridges in Chukhung crater) necessarily casts doubt upon inverted paleochannel interpretations
771 for sinuous ridges which ascend topography on Mars.

772 However, recent studies have demonstrated that the inverted paleochannel hypothesis cannot
773 necessarily be ruled out by observations of bedslope ascent by sinuous ridges (Lefort et al.,
774 2012; Williams et al., 2013). The slopes of inverted paleochannels do not necessarily reflect
775 the original slopes at the beds of ridge-forming flows, owing to spatial variations in
776 induration or armouring, post-exhumation modification (Lefort et al., 2012; Williams et al.,
777 2013), and the fact that inverted paleochannels often comprise composite deposits of
778 migratory flows (e.g., Hayden et al., 2019). Lefort et al. (2012) suggested that apparent slope
779 ascent by inverted paleochannels could result from: (1) differential modification of the
780 channel floor topography before and/or after exhumation, (2) exhumation of multiple
781 generations of paleochannels at different stratigraphic levels, (3) differential erosion of the
782 surrounding region, (4) differential settling and/or compaction of materials underlying the
783 ridge, (5) tectonic deformation, and/or (6) igneous intrusion(s) into the substrate.

784 Some of the mechanisms identified by Lefort et al. (2012) could, to some extent, explain the
785 ascent of bedslopes by the southern sinuous ridges in Chukhung crater. For example, it is
786 possible that the appearance of a ~7 m ascent of a valley wall by the S1 ridge in Figure 17A–
787 C is an outcome of differential erosion of valley-filling materials surrounding the ridge
788 during exhumation. In the cross-sectional topographic profile of the ridge in Figure 17E, the
789 base of the eastern flank of the ridge is ~10 m higher in elevation than the western flank. It is

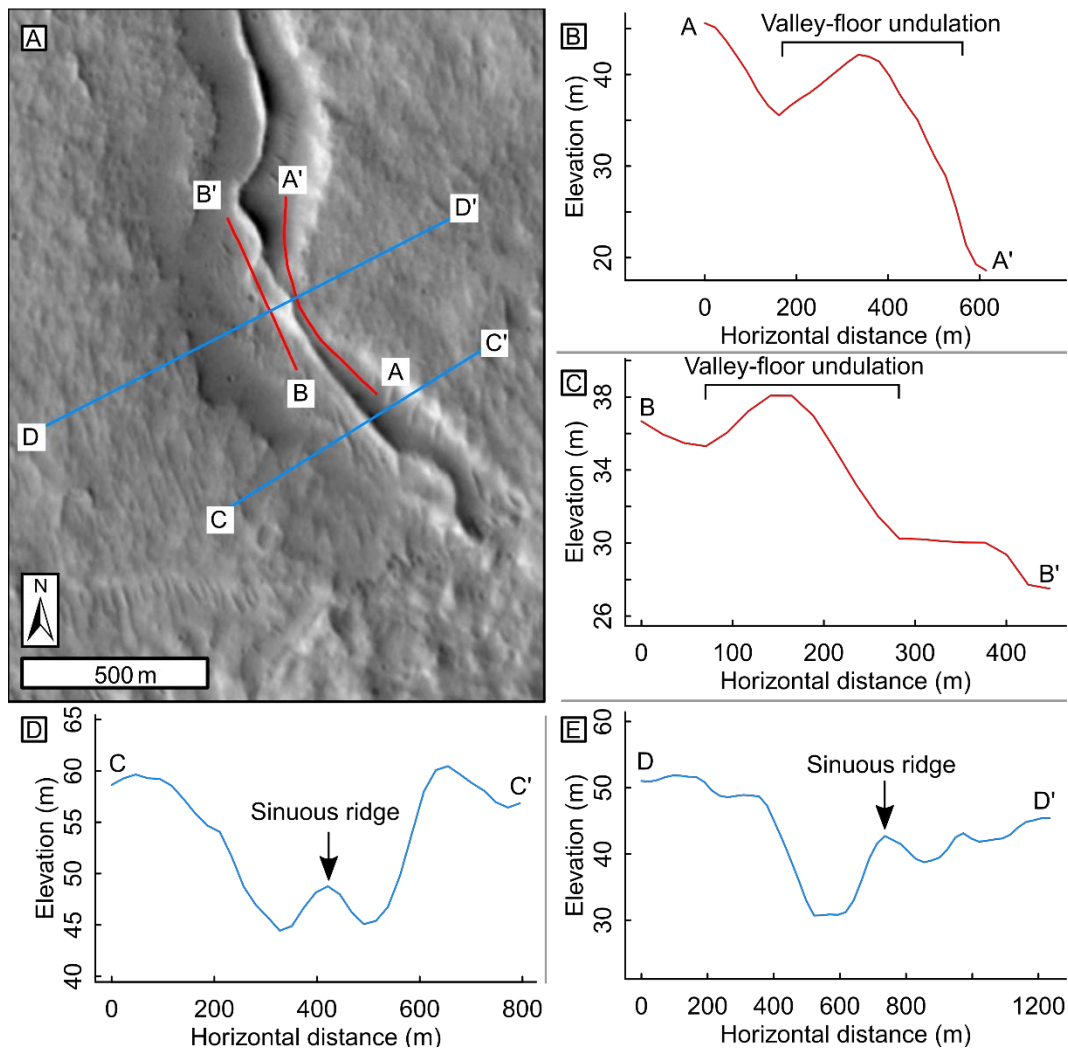


Figure 17. The possible role of differential erosion in the ascent of present-day bedslopes by sinuous ridges in Chukhung crater. (A) CTX image of an S1-type sinuous ridge in southern Chukhung crater (location in Figure 7). It appears to ascend ~7 m up the wall of the valley it occupies. Colored lines show locations of topographic profiles (obtained from the CTX DEM; Table S1) in panels B–E. (B) Topographic profile A–A’ showing the ~7 m along-ridge undulation in the present-day topography of the valley to the east of the sinuous ridge. (C) Topographic profile B–B’ showing the along-ridge undulation in the present-day topography of the valley to the west of the sinuous ridge. (D) Valley-transverse topographic profile C–C’ showing the sinuous ridge where it occupies the bottom of the valley floor. (E) Valley-transverse topographic profile D–D’ showing the sinuous ridge where it appears to be ‘perched’ part way up the valley floor. It should be noted that the width of the sinuous ridge approaches the 24 m/pixel horizontal resolution of the CTX DEM available for this location. See Table S1 for data products.

791 possible that material was preferentially eroded from the valley floor to the west of the ridge,
792 and that materials to the east of the ridge have been preferentially preserved. As such, ascent
793 of bedslopes by the S1-type sinuous ridge in Figure 17 is not necessarily uniquely indicative
794 of an esker origin.

795 The sharp-crested S2-type sinuous ridges that superpose the flat-topped S1-type sinuous
796 ridges in Figure 9E could represent locations where differential erosion and/or compaction of
797 inverted paleochannels at different stratigraphic levels gives the impression that flows
798 forming stratigraphically-higher ridges ascended paleo-bedslopes.

799 Under the slope-modification mechanisms outlined by Lefort et al. (2012) it is, however,
800 harder to explain the observation that S2 ridges occasionally exit the valley sides and cross
801 onto the adjacent plains. The deposits comprising the S2 ridges could have formed at the
802 elevation of the valley-adjacent plains at a time when the underlying valleys were buried, and
803 could have subsequently been lowered into the valleys by preferential compaction of valley-
804 filling materials. However, in some locations where S2 ridges cross over the valley sides, the
805 portions of the ridges occupying the valley floors are significantly smaller in scale (typically
806 <5 m high) than the relief of the valley walls (~25–30 m) they ascend. Thus compaction of
807 materials beneath the portions of the S2 ridges that occupy the valley floors would require the
808 emplacement and subsequent removal of a significant thickness of material atop the ridges.
809 We find no evidence for such burial and subsequent exhumation. We consider the crossing of
810 the S2 ridges out of valleys and on to valley-adjacent plains to provide the most robust
811 evidence for esker origins of these ridges.

812 6.4.3 3D morphometry

813 The southern sinuous ridges in Chukhung crater have typical heights and widths that are
814 comparable to those of VFF-linked sinuous ridges in Phlegra Montes and NW Tempe Terra

815 (Butcher, 2019; Butcher et al., 2020). This suggests that they could share a common
816 formation mechanism. However, the southern sinuous ridges (particularly the S2 type ridges)
817 appear to be morphometrically similar to the N2 type ridges on the northern floor.
818 Additionally, there is limited existing knowledge of the morphometries of inverted
819 paleochannels on Earth, or of sinuous ridges on Mars for which there is general consensus for
820 inverted paleochannel origins. The same is true for eskers; no systematic survey of the 3D
821 morphometries of a large sample of eskers on Earth has yet been completed. Thus, it is not
822 yet known whether inverted paleochannels and eskers on either Earth or Mars have distinct
823 morphometric signatures which can be used to diagnose an esker origin. Our ongoing
824 systematic morphometric analyses of sinuous ridges in Chukhung crater and elsewhere on
825 both Mars (e.g., Butcher et al., 2020) and Earth, will provide better insight into the
826 morphometric signatures of sinuous ridges in Chukhung crater and elsewhere on Mars and
827 Earth.

828 6.4.4 Sinuosity

829 Several workers have invoked differences between the typical sinuosities of eskers and rivers
830 on Earth to distinguish between esker and inverted paleochannel origins for sinuous ridges on
831 Mars (Metzger, 1992; Kargel, 1993; Banks et al., 2009; Burr et al., 2009; Williams et al.,
832 2013; Kress and Head, 2015; Butcher et al., 2016). Eskers in Canada typically have low
833 sinuosities, with median values <1.1 (Storrar et al., 2014), while meandering rivers typically
834 have sinuosities >1.3 (Schumm, 1963). In this regard, some of the S2 sinuous ridges are
835 somewhat atypical of eskers on Earth, having sinuosities up to ~ 1.6 , while the S1 sinuous
836 ridges have sinuosities that are more similar to eskers on Earth, with values up to ~ 1.2 .
837 However, specific sinuosity ranges are not unique to either eskers or inverted paleochannels
838 on Earth. For example, eskers in Canada (Storrar et al., 2014) have sinuosities ranging up to
839 2.62 (i.e. higher than the sinuosity of the S2 ridges), albeit very rarely. High (i.e. >1.3)

840 sinuosities are most common, though still unusual, among the Canadian eskers with length
841 scales similar to those in Chukhung crater (a few kilometers; Storrar et al., 2014). Similarly,
842 many subaerial rivers have sinuosities lower than 1.3; indeed, four of the five inverted
843 paleochannels measured by Maizels (1987) in Oman had sinuosities <1.1 , similar to typical
844 sinuosity values recorded by Storrar et al. (2014) for eskers in Canada. Thus, sinuosity cannot
845 necessarily be used to reliably distinguish between eskers and inverted paleochannels.

846 6.5 Proposed Origins of Sinuous Ridges in Chukhung Crater

847 We are confident that the N1-type sinuous ridges in Chukhung crater are inverted
848 paleochannels based on their associations with valleys on the crater walls and within the
849 upper incised plains unit (e.g., Figure 10), relationships to possible resistant materials in the
850 upper plains and ridges unit, evidence for flow migration (Figure 11) and extensive
851 subsequent landscape deflation, and a lack of evidence for either past or present glaciation on
852 the northern walls or floor of Chukhung crater. The alignment of some N2 ridges with the
853 downslope ends of some N1 type ridges, and their lack of spatial association with units of
854 inferred glacial origin suggests that they are also more likely to be inverted paleochannels.
855 However, the interpretation of the N2 ridges as inverted paleochannels is less certain than
856 that for the N1 ridges.

857 The origins of the southern sinuous ridges are ambiguous; there is evidence to support both
858 esker and inverted paleochannel origins. They are associated with (and commonly emerge
859 from) glacial deposits including extant VFFs (putative debris-covered glaciers) and
860 moraine-like units, and have numerous esker-like characteristics. However, many of these
861 characteristics could also be explained under the inverted paleochannel hypothesis. The
862 associations between the S1 ridges and non-glacial units in the southern Chukhung crater are
863 similar to those of the N1 (i.e. inverted paleochannel-like) ridges, such that it is possible that
864 both the N1 and S1 ridges are inverted paleochannels. Importantly, however, the relationships

865 of the S2 ridges to non-glacial units (i.e. the fact that the S2 ridges commonly ascend valley
866 walls and cross onto valley-adjacent plateaus) is harder to explain under the inverted
867 paleochannel hypothesis. Thus, among the sinuous ridges in Chukhung crater, S2 ridges are
868 the strongest candidates as eskers. Notable morphologic similarities between N2 and S2
869 ridges means that we also do not rule out esker origins for the N2 ridges.

870 Given our confidence that the N1 sinuous ridges are inverted paleochannels, it is very
871 unlikely that all sinuous ridges in Chukhung crater are eskers. Based on the balance of
872 evidence presented here, we consider the most probable scenarios to be either that: (Scenario
873 1), the N1, N2, and S1 ridges are inverted paleochannels, and the S2 ridges are eskers; or
874 (Scenario 2), that the northern sinuous ridges are inverted paleochannels, and the southern
875 sinuous ridges are eskers. Other possible scenarios that we consider to be less likely, but
876 which warrant further investigation, include: (Scenario 3) that all sinuous ridges in
877 Chukhung crater are inverted paleochannels; (Scenario 4), that the N1 ridges are inverted
878 paleochannels, and the N2, S1, and S2 ridges are eskers; and (Scenario 5), that the N1 and S1
879 ridges are inverted paleochannels, and that the N2 and S2 ridges are eskers. Ongoing detailed
880 morphometric analyses of sinuous ridges in Chukhung crater, and comparisons to analogous
881 landforms on both Earth and Mars aim to test Scenarios 1–5 further. Scenario 3 would require
882 additional explanation for how sinuous ridges could cross out of their host valleys under the
883 inverted paleochannel hypothesis, while scenarios 4 and 5 would require an explanation for
884 the apparent asymmetry in the preservation of glacial deposits between the northern and
885 southern portions of Chukhung crater.

886 **7. Paleoenvironmental Implications**

887 Regardless of which of the scenarios outlined in Section 6.5 is true, sinuous ridges in
888 Chukhung crater represent protracted and/or episodic periods of wet conditions (subaerially,

889 and possibly also subglacially) between the early Hesperian and mid Amazonian (~3.6–
890 2.1 Ga; Section 5.7). Chukhung crater is one of a growing number of case studies
891 demonstrating the occurrence of post-Noachian fluvial activity within impact craters on Mars
892 (e.g., Grant and Wilson, 2011; Mangold et al., 2012; Kite et al., 2017; Vijayan et al., 2020).

893 Multi-stage subaerial fluvial drainage which formed the N1 ridges (including features
894 suggestive of channel migration; Figure 11) in Chukhung crater is consistent with the
895 interpretations of Peel and Fassett (2013), that many central pit craters on Mars probably
896 experienced protracted fluvial activity during the Hesperian or Amazonian. The ~3.6–2.1 Ga
897 age envelope that we have modeled for Chukhung crater is consistent with the observations
898 of Peel and Fassett (2013), and with the occurrence of fluvial activity in Chukhung crater
899 after the period of major valley network formation on Mars (e.g., Fassett and Head, 2008;
900 Hynek et al., 2010).

901 Under scenarios 1, 2, and 3 outlined in Section 6.5, notable differences in sinuosity between
902 ridge populations interpreted as inverted paleochannels could suggest that hydraulic
903 conditions of subaerial drainage in Chukhung crater varied through time. Maizels (1987)
904 invoked increased grain size of entrained sediments, and increases in peak flow depths and
905 velocities to explain the decrease in sinuosity between stratigraphically-lower (i.e. older, with
906 sinuosities of >1.7) and stratigraphically-higher (i.e., younger, with sinuosities of ~1.03)
907 inverted paleochannels in Oman. The increase in typical sinuosities between older (e.g., N1
908 and S1) and younger (e.g., S2 and N2) sinuous ridges in Chukhung crater is of similar
909 magnitude but the opposite sense (i.e., an increase in sinuosity towards stratigraphically-
910 higher ridges) to that observed by Maizels (1987). If the ridges are inverted paleochannels,
911 this could be explained by reductions in sediment grain size, flow depths, and velocities
912 towards later subaerial drainage events. Factors that could have promoted such transitions
913 include: reductions in the slope of the crater wall and floor due to relaxation and/or infilling

914 of crater topography, reductions in sediment supply and/or flow power under drying climate
915 conditions, or alternatively an increase in hydraulic base level (e.g., the flow depth of a
916 possible lake in the central pit) under wetter climate conditions.

917 If any of the sinuous ridges in Chukhung crater are eskers, the location of the crater within an
918 extensive tectonic rift system is consistent with the growing body of evidence (Gallagher and
919 Balme, 2015; Butcher et al., 2017; Arnold et al., 2019; Sori and Bramson, 2019) that elevated
920 geothermal heat flux was a pre-requisite for recent wet-based glaciation on Mars.

921 Considering the uncertainties discussed in Section 5.7.2, the best-fit model age obtained for
922 LDAs in Chukhung crater (330 ± 90 Ma) suggests that the LDA formation, and therefore a
923 possible esker-forming melt episode, could have occurred at a broadly similar time to esker-
924 forming melt episodes in glaciated tectonic rifts/graben in NW Tempe Terra ($\sim 110 \pm 10$ Ma;
925 Butcher et al., 2017) and Phlegra Montes ($\sim 150 \pm 20$ Ma; Gallagher and Balme, 2015).

926 Although the Tempe Fossae rift system and associated volcanic constructs are thought to
927 have ceased major activity during the late Hesperian (Hauber and Kronberg, 2001; Hauber et
928 al., 2010), we cannot exclude the possibility of late-stage subsurface activity associated with
929 this system continued into the Amazonian. Further investigation of the tectonic and volcanic
930 history of the wider region could aid understanding of possible geothermal influences upon
931 mid- to late-Amazonian glacial melting in Chukhung crater. It should be noted that numerical
932 modeling experiments suggest that for basal melting to have occurred during the Amazonian
933 period, geothermal heating would need to be supplemented by other drivers such as viscous
934 strain heating within glacial ice, small-magnitude climate warming, and/or melting point
935 depression by salts (Butcher et al., 2017; Sori and Bramson, 2019). Mid-latitude climate
936 fluctuations during the Amazonian (see Figure 7 in Haberle et al., 2003) were probably
937 insufficient to have operated alone in inducing basal melting of glacial ice deposits.

938 Finally, if the N2 sinuous ridges are eskers (Scenarios 4 and 5 in Section 6.5, which we
939 consider to be the least likely of Scenarios 1–5), or our interpretation of the LDA-terminal
940 lobes as moraines is incorrect (our leading alternative hypothesis being that they are impact
941 ejecta), candidate eskers in Chukhung crater could be the product of an earlier glaciation
942 predating the extant LDA and LDA-terminal lobes in Chukhung crater. If the LDA-terminal
943 lobes are impact ejecta from the SE rayed crater, our best-fit model age for the SE rayed
944 crater would provide a minimum bounding age of 2.1 Ga for esker formation in Chukhung
945 crater. However, our analyses suggest that the LDA-terminal moraines are more likely to be
946 moraines than impact ejecta, and that the N2 ridges are more likely to be inverted
947 paleochannels than eskers.

948 **8. Conclusions**

949 Chukhung crater, Mars, has undergone complex geologic evolution since its formation
950 between the early Hesperian and early Amazonian periods. Its interior has been modified by
951 subaerial (and possibly subglacial) flows of liquid water, glaciation, and extensive landscape
952 erosion. Sinuous ridges in northern Chukhung crater are best explained as inverted
953 paleochannels comprising exhumed fluvial sediments deposited by subaerial flows of water
954 draining from the northern crater wall. Sinuous ridges in southern Chukhung crater emerge
955 from the terminal deposits of extant debris-covered glaciers. Esker-like characteristics of S1-
956 type sinuous ridges, which occupy crater-floor valleys, could be explained under either the
957 esker or inverted paleochannel hypothesis, hence we are uncertain about their origins. S2-
958 type sinuous ridges in southern Chukhung crater are the strongest esker candidates in
959 Chukhung crater; existing explanations for the apparent ascent of topography by inverted
960 paleochannels cannot adequately explain the fact that the S2 sinuous ridges commonly ascend
961 relatively high-relief walls of crater-floor valleys and cross onto valley-adjacent plains. To
962 summarise we are confident that the N1 sinuous ridges are inverted paleochannels, and

963 consider it most likely that the N2 sinuous ridges are also inverted paleochannels. The
964 inverted paleochannel and esker hypotheses provide similarly strong explanations for the S1-
965 type sinuous ridges, but we find that the esker hypothesis provides a better explanation for the
966 properties of the S2 sinuous ridges.

967 Chukhung crater provides a valuable case study highlighting several challenges that remain
968 for the identification of eskers on Mars. Esker identification is complicated by similarities in
969 form between eskers and inverted paleochannels. Confidence that a sinuous ridge on Mars is
970 an esker can be significantly improved if that sinuous ridge is associated with extant ice
971 deposits such as VFFs, and there is no associated evidence for deflation or topographic
972 inversion of the surrounding landscape. However, in locations such as Chukhung crater,
973 landsystems that are consistent with both esker and inverted paleochannel origins coexist in
974 close proximity. This complicates definitive interpretation of VFF-linked sinuous ridges as
975 eskers and explains, in particular, our caution over the interpretation of the S1 ridges (which
976 emerge from beneath glacial deposits and appear esker-like, but have no apparent
977 characteristics that cannot also be explained under the inverted paleochannel hypothesis).

978 Sinuous ridges interpreted as inverted paleochannels in northern and possibly also southern
979 Chukhung crater provide evidence for multiple prolonged episodes of distributed, possibly
980 precipitation- or snowmelt-driven, subaerial fluvial activity and sedimentary aggradation
981 between the early Hesperian and mid Amazonian (Peel and Fassett, 2013). Thus, Chukhung
982 crater or the wider central Tempe Terra region probably experienced climate conditions that
983 were unusually warm and wet compared to the generally cold and dry climate conditions that
984 are thought to have prevailed during that time period.

985 If the southern sinuous ridges (S2-type and possibly also S1-type) in Chukhung crater are
986 eskers formed by basal melting of mid- to late-Amazonian-aged glaciers in Chukhung crater,

987 their location in a tectonic rift zone is consistent with the possible influence of geothermal
988 heating upon basal melting of their parent glaciers. However, further analyses of the regional
989 tectono-magmatic history are required to assess the likelihood that elevated geothermal heat
990 flux persisted into the period following glacial advance within Chukhung crater.

991 **9. Acknowledgements**

992 We are grateful to two anonymous reviewers for thoughtful reviews on this manuscript. This
993 work was undertaken at the Open University as part of a PhD studentship held by FEGB and
994 funded by the Science and Technology Facilities Council (STFC) grant ST/N50421X/1.
995 Manuscript preparation was undertaken when FEGB was part of the PALGLAC research
996 team, supported by the European Research Council (ERC) under the European Union's
997 Horizon 2020 research and innovation programme (Grant agreement No. 787263). We also
998 gratefully acknowledge UK Space Agency grants ST/L00643X/1, ST/R001413/1, and
999 ST/R001383/1 (MRB); ST/R001405/1, ST/P001262/1, and ST/S00145X/1 (SRL);
1000 ST/R/001375 (AH); and ST/R002355/1 (JMD). SJC is supported by the French space agency,
1001 CNES. We thank David Mayer and Edwin Kite (Mayer and Kite, 2016) for generating and
1002 sharing CTX and HiRISE digital elevation models used in this study. We also thank Edwin
1003 Kite and Caleb Fassett for drawing our attention to the study area.

1004 **10. References**

- 1005 Arnold, N.S., Conway, S.J., Butcher, F.E.G., Balme, M.R., 2019. Modeled Subglacial Water
1006 Flow Routing Supports Localized Intrusive Heating as a Possible Cause of Basal
1007 Melting of Mars' South Polar Ice Cap. *Journal of Geophysical Research: Planets* 124,
1008 2101–2116. <https://doi.org/10.1029/2019JE006061>
1009 Aylsworth, J.M., Shilts, W.W., 1989. Glacial features around the Keewatin ice divide: districts
1010 of Mackenzie and Keewatin, Geological Survey of Canada, Map 24-1987, scale
1011 1:1,000,000.
1012 Baker, D.M.H., Carter, L.M., 2019. Probing supraglacial debris on Mars 2: Crater morphology.
1013 *Icarus* 319, 264–280. <https://doi.org/10.1016/j.icarus.2018.09.009>

1014 Balme, M., Berman, D.C., Bourke, M.C., Zimbelman, J.R., 2008. Transverse Aeolian Ridges
1015 (TARs) on Mars. *Geomorphology* 101, 703–720.
1016 <https://doi.org/10.1016/j.geomorph.2008.03.011>

1017 Balme, M.R., Gupta, S., Davis, J.M., Fawdon, P., Grindrod, P.M., Bridges, J.C., Sefton-Nash,
1018 E., Williams, R.M.E., 2020. Aram Dorsum: An Extensive Mid-Noachian Age Fluvial
1019 Depositional System in Arabia Terra, Mars. *Journal of Geophysical Research: Planets*
1020 125, e2019JE006244. <https://doi.org/10.1029/2019JE006244>

1021 Banks, M.E., Lang, N.P., Kargel, J.S., McEwen, A.S., Baker, V.R., Grant, J.A., Pelletier, J.D.,
1022 Strom, R.G., 2009. An analysis of sinuous ridges in the southern Argyre Planitia, Mars
1023 using HiRISE and CTX images and MOLA data. *J. Geophys. Res.* 114, E09003.
1024 <https://doi.org/10.1029/2008JE003244>

1025 Burke, M.J., Brennand, T.A., Perkins, A.J., 2012. Transient subglacial hydrology of a thin ice
1026 sheet: insights from the Chasm esker, British Columbia, Canada. *Quaternary Science*
1027 *Reviews* 58, 30–55. <https://doi.org/10.1016/j.quascirev.2012.09.004>

1028 Burr, D.M., Enga, M.-T., Williams, R.M.E., Zimbelman, J.R., Howard, A.D., Brennand, T.A.,
1029 2009. Pervasive aqueous paleoflow features in the Aeolis/Zephyria Plana region, Mars.
1030 *Icarus* 200, 52–76. <https://doi.org/10.1016/j.icarus.2008.10.014>

1031 Butcher, F.E.G., 2019. Wet-Based Glaciation on Mars (PhD Thesis). The Open University,
1032 Milton Keynes, UK. <http://oro.open.ac.uk/id/eprint/60703>.

1033 Butcher, F.E.G., Balme, M.R., Conway, S.J., Gallagher, C., Arnold, N.S., Storrar, R.D., Lewis,
1034 S.R., Hagermann, A., 2020. Morphometry of a glacier-linked esker in NW Tempe
1035 Terra, Mars, and implications for sediment-discharge dynamics of subglacial drainage.
1036 *Earth and Planetary Science Letters* 542, 116325.
1037 <https://doi.org/10.1016/j.epsl.2020.116325>

1038 Butcher, F.E.G., Balme, M.R., Gallagher, C., Arnold, N.S., Conway, S.J., Hagermann, A.,
1039 Lewis, S.R., 2017. Recent Basal Melting of a Mid-Latitude Glacier on Mars. *J.*
1040 *Geophys. Res. Planets* 122, 2445–2468. <https://doi.org/10.1002/2017JE005434>

1041 Butcher, F.E.G., Conway, S.J., Arnold, N.S., 2016. Are the Dorsa Argentea on Mars eskers?
1042 *Icarus* 275, 65–84. <https://doi.org/10.1016/j.icarus.2016.03.028>

1043 Cardenas, B.T., Mohrig, D., Goudge, T.A., 2018. Fluvial stratigraphy of valley fills at Aeolis
1044 Dorsa, Mars: Evidence for base-level fluctuations controlled by a downstream water
1045 body. *GSA Bulletin* 130, 484–498. <https://doi.org/10.1130/B31567.1>

1046 Christensen, P.R., Jakosky, B.M., Kieffer, H.H., Malin, M.C., McSween Jr, H.Y., Nealson, K.,
1047 Mehall, G.L., Silverman, S.H., Ferry, S., Caplinger, M., Ravine, M., 2004. The Thermal
1048 Emission Imaging System (THEMIS) for the Mars 2001 Odyssey Mission. *Space*
1049 *Science Reviews* 110, 85–130.
1050 <https://doi.org/doi:10.1023/B:SPAC.0000021008.16305.94>

1051 Chuang, F.C., Williams, R.M.E., 2018. Valley network morphology in the greater Meridiani
1052 Planum region, Mars. *Journal of Maps* 14, 652–660.
1053 <https://doi.org/10.1080/17445647.2018.1530154>

1054 Davis, J.M., Gupta, S., Balme, M., Grindrod, P.M., Fawdon, P., Dickeson, Z.I., Williams,
1055 R.M.E., 2019. A Diverse Array of Fluvial Depositional Systems in Arabia Terra:
1056 Evidence for mid-Noachian to Early Hesperian Rivers on Mars. *Journal of Geophysical*
1057 *Research: Planets* 124, 1913–1934. <https://doi.org/10.1029/2019JE005976>

1058 Edwards, C.S., Nowicki, K.J., Christensen, P.R., Hill, J., Gorelick, N., Murray, K., 2011.
1059 Mosaicking of global planetary image datasets: 1. Techniques and data processing for
1060 Thermal Emission Imaging System (THEMIS) multi-spectral data. *J. Geophys. Res.*
1061 116, E10008. <https://doi.org/10.1029/2010JE003755>

1062 Fassett, C.I., Head, J.W., 2008. The timing of martian valley network activity: Constraints from
1063 buffered crater counting. *Icarus* 195, 61–89.
1064 <https://doi.org/10.1016/j.icarus.2007.12.009>

1065 Gallagher, C., Balme, M., 2015. Eskers in a complete, wet-based glacial system in the Phlegra
1066 Montes region, Mars. *Earth and Planetary Science Letters* 431, 96–109.
1067 <https://doi.org/10.1016/j.epsl.2015.09.023>

1068 Grant, J.A., Wilson, S.A., 2011. Late alluvial fan formation in southern Margaritifer Terra,
1069 Mars. *Geophysical Research Letters* 38. <https://doi.org/10.1029/2011GL046844>

1070 Haberle, R.M., Murphy, J.R., Schaeffer, J., 2003. Orbital change experiments with a Mars
1071 general circulation model. *Icarus* 161, 66–89. <https://doi.org/10.1016/S0019->
1072 [1035\(02\)00017-9](https://doi.org/10.1016/S0019-1035(02)00017-9)

1073 Hambrey, M.J., Huddart, D., Bennett, M.R., Glasser, N.F., 1997. Genesis of ‘hummocky
1074 moraines’ by thrusting in glacier ice: evidence from Svalbard and Britain. *Journal of*
1075 *the Geological Society* 154, 623–632. <https://doi.org/10.1144/gsjgs.154.4.0623>

1076 Hartmann, W.K., 2005. Martian cratering 8: Isochron refinement and the chronology of Mars.
1077 *Icarus* 174, 294–320. <https://doi.org/10.1016/j.icarus.2004.11.023>

1078 Hartmann, W.K., Neukum, G., 2001. Cratering Chronology and the Evolution of Mars. *Space*
1079 *Science Reviews* 96, 165–194. <https://doi.org/10.1023/A:1011945222010>

1080 Hauber, E., Grott, M., Kronberg, P., 2010. Martian rifts: Structural geology and geophysics.
1081 *Earth and Planetary Science Letters* 294, 393–410.
1082 <https://doi.org/10.1016/j.epsl.2009.11.005>

1083 Hauber, E., Kronberg, P., 2001. Tempe Fossae, Mars: A planetary analogon to a terrestrial
1084 continental rift? *J. Geophys. Res.* 106, 20587–20602.
1085 <https://doi.org/10.1029/2000JE001346>

1086 Hayden, A.T., Lamb, M.P., Fischer, W.W., Ewing, R.C., McElroy, B.J., Williams, R.M.E.,
1087 2019. Formation of sinuous ridges by inversion of river-channel belts in Utah, USA,
1088 with implications for Mars. *Icarus* 332, 92–110.
1089 <https://doi.org/10.1016/j.icarus.2019.04.019>

1090 Head, J.W., 2000a. Tests for Ancient Polar Deposits on Mars: Origin of Esker-like Sinuous
1091 Ridges (Dorsa Argentea) Using MOLA Data. Lunar and Planetary Science Conference
1092 XXXI. Abstract #1116.

1093 Head, J.W., 2000b. Tests for Ancient Polar Deposits on Mars: Morphology and Topographic
1094 Relationships of Esker-like Sinuous Ridges (Dorsa Argentea) Using MOLA Data.
1095 Lunar and Planetary Science Conference XXXI. Abstract #1117.

1096 Head, J.W., Hallet, B., 2001a. Origin of Sinuous Ridges in the Dorsa Argentea Formation: New
1097 Observations and Tests of the Esker Hypothesis. Lunar and Planetary Science
1098 Conference XXXII. Abstract #1373.

1099 Head, J.W., Hallet, B., 2001b. Origin of Sinuous Ridges in the Dorsa Argentea Formation:
1100 Additional Criteria for Tests of the Esker Hypothesis. Lunar and Planetary Science
1101 Conference XXXII. Abstract #1366.

1102 Head, J.W., Marchant, D.R., Dickson, J.L., Kress, A.M., Baker, D.M., 2010. Northern mid-
1103 latitude glaciation in the Late Amazonian period of Mars: Criteria for the recognition
1104 of debris-covered glacier and valley glacier landsystem deposits. *Earth and Planetary*
1105 *Science Letters* 294, 306–320. <https://doi.org/10.1016/j.epsl.2009.06.041>

1106 Holt, J.W., Safaeinili, A., Plaut, J.J., Head, J.W., Phillips, R.J., Seu, R., Kempf, S.D.,
1107 Choudhary, P., Young, D.A., Putzig, N.E., Biccari, D., Gim, Y., 2008. Radar Sounding
1108 Evidence for Buried Glaciers in the Southern Mid-Latitudes of Mars. *Science* 322,
1109 1235–1238. <https://doi.org/10.1126/science.1164246>

1110 Howard, A.D., 1981. Etched plains and braided ridges of the south polar region of Mars:
1111 Features produced by basal melting of ground ice? *Reports of Planetary Geology*

1112 Program 1981: National Aeronautics and Space Administration Technical
1113 Memorandum 84211, 286–288.

1114 Hynek, B.M., Beach, M., Hoke, M.R.T., 2010. Updated global map of Martian valley networks
1115 and implications for climate and hydrologic processes. *J. Geophys. Res.* 115, E09008.
1116 <https://doi.org/10.1029/2009JE003548>

1117 Ivanov, B.A., 2001. Mars/Moon Cratering Rate Ratio Estimates. *Space Science Reviews* 96,
1118 87–104. <https://doi.org/10.1023/A:1011941121102>

1119 Jaumann, R., Neukum, G., Behnke, T., Duxbury, T.C., Eichentopf, K., Flohrer, J., Gasselt, S.
1120 v., Giese, B., Gwinner, K., Hauber, E., Hoffmann, H., Hoffmeister, A., Köhler, U.,
1121 Matz, K.-D., McCord, T.B., Mertens, V., Oberst, J., Pischel, R., Reiss, D., Ress, E.,
1122 Roatsch, T., Saiger, P., Scholten, F., Schwarz, G., Stephan, K., Wählisch, M., 2007.
1123 The high-resolution stereo camera (HRSC) experiment on Mars Express: Instrument
1124 aspects and experiment conduct from interplanetary cruise through the nominal
1125 mission. *Planetary and Space Science* 55, 928–952.
1126 <https://doi.org/10.1016/j.pss.2006.12.003>

1127 Kargel, J.S., 1993. Geomorphic processes in the Argyre-Dorsa Argentea region of Mars. *Lunar*
1128 *and Planetary Science Conference XXIV. Abstract #1378.*

1129 Kargel, J.S., Strom, R.G., 1992. Ancient glaciation on Mars. *Geology* 20, 3–7.
1130 [https://doi.org/10.1130/0091-7613\(1992\)020<0003:AGOM>2.3.CO;2](https://doi.org/10.1130/0091-7613(1992)020<0003:AGOM>2.3.CO;2)

1131 Kehew, A.E., Piotrowski, J.A., Jørgensen, F., 2012. Tunnel valleys: Concepts and
1132 controversies — A review. *Earth-Science Reviews* 113, 33–58.
1133 <https://doi.org/10.1016/j.earscirev.2012.02.002>

1134 Kite, E.S., Sneed, J., Mayer, D.P., Wilson, S.A., 2017. Persistent or repeated surface
1135 habitability on Mars during the late Hesperian - Amazonian. *Geophysical Research*
1136 *Letters* 44, 3991–3999. <https://doi.org/10.1002/2017GL072660>

1137 Kneissl, T., van Gasselt, S., Neukum, G., 2011. Map-projection-independent crater size-
1138 frequency determination in GIS environments—New software tool for ArcGIS.
1139 *Planetary and Space Science* 59, 1243–1254. <https://doi.org/10.1016/j.pss.2010.03.015>

1140 Kress, A.M., Head, J.W., 2015. Late Noachian and early Hesperian ridge systems in the south
1141 circumpolar Dorsa Argentea Formation, Mars: Evidence for two stages of melting of
1142 an extensive late Noachian ice sheet. *Planetary and Space Science* 109–110, 1–20.
1143 <https://doi.org/10.1016/j.pss.2014.11.025>

1144 Krüger, J., Kjær, K.H., 2000. De-icing progression of ice-cored moraines in a humid, subpolar
1145 climate, Kötlujökull, Iceland. *The Holocene* 10, 737–747.
1146 <https://doi.org/10.1191/09596830094980>

1147 Lefort, A., Burr, D.M., Beyer, R.A., Howard, A.D., 2012. Inverted fluvial features in the
1148 Aeolis-Zephyria Plana, western Medusae Fossae Formation, Mars: Evidence for post-
1149 formation modification. *Journal of Geophysical Research: Planets* 117, E03007.
1150 <https://doi.org/10.1029/2011JE004008>

1151 Maizels, J.K., 1987. Plio-Pleistocene raised channel systems of the western Sharqiya (Wahiba),
1152 Oman. *Geological Society, London, Special Publications* 35, 31–50.
1153 <https://doi.org/10.1144/GSL.SP.1987.035.01.04>

1154 Malin, M.C., Bell, J.F., Cantor, B.A., Caplinger, M.A., Calvin, W.M., Clancy, R.T., Edgett,
1155 K.S., Edwards, L., Haberle, R.M., James, P.B., Lee, S.W., Ravine, M.A., Thomas, P.C.,
1156 Wolff, M.J., 2007. Context Camera Investigation on board the Mars Reconnaissance
1157 Orbiter. *J. Geophys. Res.* 112, E05S04. <https://doi.org/10.1029/2006JE002808>

1158 Mangold, N., Adeli, S., Conway, S., Ansan, V., Langlais, B., 2012. A chronology of early Mars
1159 climatic evolution from impact crater degradation. *Journal of Geophysical Research:*
1160 *Planets* 117. <https://doi.org/10.1029/2011JE004005>

- 1161 Masursky, H., Boyce, J.M., Dial, A.L., Schaber, G.G., Strobell, M.E., 1977. Classification and
1162 time of formation of Martian channels based on Viking data. *Journal of Geophysical*
1163 *Research* 82, 4016–4038. <https://doi.org/10.1029/JS082i028p04016>
- 1164 Mayer, D.P., Kite, E.S., 2016. An Integrated Workflow for Producing Digital Terrain Models
1165 of Mars from CTX and HiRISE Stereo Data Using the NASA Ames Stereo Pipeline.
1166 Lunar and Planetary Science Conference XLVII Abstract #1241.
- 1167 McEwen, A.S., Eliason, E.M., Bergstrom, J.W., Bridges, N.T., Hansen, C.J., Delamere, W.A.,
1168 Grant, J.A., Gulick, V.C., Herkenhoff, K.E., Keszthelyi, L., Kirk, R.L., Mellon, M.T.,
1169 Squyres, S.W., Thomas, N., Weitz, C.M., 2007. Mars Reconnaissance Orbiter’s High
1170 Resolution Imaging Science Experiment (HiRISE). *Journal of Geophysical Research*
1171 112, E05S02. <https://doi.org/10.1029/2005JE002605>
- 1172 Metzger, S.M., 1992. The Eskers of New York State: Formation Process Implications and
1173 Esker-like Features on the Planet Mars. Lunar and Planetary Science Conference XXIII.
1174 Abstract #1448.
- 1175 Michael, G.G., Platz, T., Kneissl, T., Schmedemann, N., 2012. Planetary surface dating from
1176 crater size–frequency distribution measurements: Spatial randomness and clustering.
1177 *Icarus* 218, 169–177. <https://doi.org/10.1016/j.icarus.2011.11.033>
- 1178 Neukum, G., Jaumann, R., the HRSC Co-Investigator and Experiment Team, 2004. HRSC:
1179 The high resolution stereo camera of Mars Express, in: Wilson, A. (Ed.), *Mars Express:*
1180 *The Scientific Payload*, European Space Agency Special Publication 1240. pp. 17–35.
- 1181 Orosei, R., Lauro, S.E., Pettinelli, E., Cicchetti, A., Coradini, M., Cosciotti, B., Paolo, F.D.,
1182 Flamini, E., Mattei, E., Pajola, M., Soldovieri, F., Cartacci, M., Cassenti, F., Frigeri,
1183 A., Giuppi, S., Martufi, R., Masdea, A., Mitri, G., Nenna, C., Noschese, R., Restano,
1184 M., Seu, R., 2018. Radar evidence of subglacial liquid water on Mars. *Science*
1185 *ear7268*. <https://doi.org/10.1126/science.ear7268>
- 1186 Pain, C.F., Clarke, J.D.A., Thomas, M., 2007. Inversion of relief on Mars. *Icarus, Deep Impact*
1187 *Mission to Comet 9P/Tempel 1, Part 2* 190, 478–491.
1188 <https://doi.org/10.1016/j.icarus.2007.03.017>
- 1189 Pain, C.F., Oilier, C.D., 1995. Inversion of relief — a component of landscape evolution.
1190 *Geomorphology* 12, 151–165. [https://doi.org/10.1016/0169-555X\(94\)00084-5](https://doi.org/10.1016/0169-555X(94)00084-5)
- 1191 Peel, S.E., Fassett, C.I., 2013. Valleys in pit craters on Mars: Characteristics, distribution, and
1192 formation mechanisms. *Icarus* 225, 272–282.
1193 <https://doi.org/10.1016/j.icarus.2013.03.031>
- 1194 Perkins, A.J., Brennand, T.A., Burke, M.J., 2016. Towards a morphogenetic classification of
1195 eskers: Implications for modelling ice sheet hydrology. *Quaternary Science Reviews*
1196 134, 19–38. <https://doi.org/10.1016/j.quascirev.2015.12.015>
- 1197 Petersen, E.I., Holt, J.W., Levy, J.S., 2018. High Ice Purity of Martian Lobate Debris Aprons
1198 at the Regional Scale: Evidence From an Orbital Radar Sounding Survey in
1199 Deuteronilus and Protonilus Mensae. *Geophysical Research Letters* 45, 11,595–11,604.
1200 <https://doi.org/10.1029/2018GL079759>
- 1201 Plaut, J.J., Safaeinili, A., Holt, J.W., Phillips, R.J., Head, J.W., Seu, R., Putzig, N.E., Frigeri,
1202 A., 2009. Radar evidence for ice in lobate debris aprons in the mid-northern latitudes
1203 of Mars. *Geophys. Res. Lett.* 36, L02203. <https://doi.org/10.1029/2008GL036379>
- 1204 Robbins, S.J., Hynes, B.M., 2012. A new global database of Mars impact craters ≥ 1 km: 2.
1205 Global crater properties and regional variations of the simple-to-complex transition
1206 diameter. *J. Geophys. Res.* 117, E06001. <https://doi.org/10.1029/2011JE003967>
- 1207 Schumm, S.A., 1963. Sinuosity of Alluvial Rivers on the Great Plains. *GSA Bulletin* 74, 1089–
1208 1100. [https://doi.org/10.1130/0016-7606\(1963\)74\[1089:SOAROT\]2.0.CO;2](https://doi.org/10.1130/0016-7606(1963)74[1089:SOAROT]2.0.CO;2)

1209 Shreve, R.L., 1985. Esker characteristics in terms of glacier physics, Katahdin esker system,
1210 Maine. Geological Society of America Bulletin 96, 639–646.
1211 [https://doi.org/10.1130/0016-7606\(1985\)96<639:ECITOG>2.0.CO;2](https://doi.org/10.1130/0016-7606(1985)96<639:ECITOG>2.0.CO;2)
1212 Shreve, R.L., 1972. Movement of water in glaciers. Journal of Glaciology 11, 205–214.
1213 <https://doi.org/doi:10.3189/S002214300002219X>
1214 Smith, D.E., Zuber, M.T., Frey, H.V., Garvin, J.B., Head, J.W., Muhleman, D.O., Pettengill,
1215 G.H., Phillips, R.J., Solomon, S.C., Zwally, H.J., Banerdt, W.B., Duxbury, T.C.,
1216 Golombek, M.P., Lemoine, F.G., Neumann, G.A., Rowlands, D.D., Aharonson, O.,
1217 Ford, P.G., Ivanov, A.B., Johnson, C.L., McGovern, P.J., Abshire, J.B., Afzal, R.S.,
1218 Sun, X., 2001. Mars Orbiter Laser Altimeter: Experiment summary after the first year
1219 of global mapping of Mars. J. Geophys. Res. 106, 23689–23722.
1220 <https://doi.org/10.1029/2000JE001364>
1221 Sori, M., Bramson, A.M., 2019. Water on Mars, with a Grain of Salt: Local Heat Anomalies
1222 are Required for Basal Melting of Ice at the South Pole Today. Geophysical Research
1223 Letters 46, 1222–1231.
1224 Squyres, S.W., 1979. The distribution of lobate debris aprons and similar flows on Mars. J.
1225 Geophys. Res. 84, 8087–8096. <https://doi.org/10.1029/JB084iB14p08087>
1226 Storrar, R.D., Stokes, C.R., Evans, D.J.A., 2014. Morphometry and pattern of a large sample
1227 (>20,000) of Canadian eskers and implications for subglacial drainage beneath ice
1228 sheets. Quaternary Science Reviews 105, 1–25.
1229 <https://doi.org/10.1016/j.quascirev.2014.09.013>
1230 Tanaka, K.L., Kolb, E.J., 2001. Geologic History of the Polar Regions of Mars Based on Mars
1231 Global Surveyor Data I. Noachian and Hesperian Periods. Icarus 154, 3–21.
1232 <https://doi.org/10.1006/icar.2001.6675>
1233 Tanaka, K.L., Skinner, J.A., Dohm, J.M., Irwin III, R.P., Kolb, E.J., Fortezzo, C.M., Platz, T.,
1234 Michael, G.G., Hare, T., 2014a. Geologic Map of Mars, US Geologic Survey Scientific
1235 Investigations Map 3292, scale 1:20,000,000, with 43 p. pamphlet.
1236 Tanaka, K.L., Skinner, J.A., Dohm, J.M., Irwin III, R.P., Kolb, E.J., Fortezzo, C.M., Platz, T.,
1237 Michael, G.G., Hare, T., 2014b. Geologic map of Mars, Pamphlet to accompany
1238 Scientific Investigations Map 3292. US Geological Survey.
1239 Vijayan, S., Sinha, R.K., Harish, Anilkumar, R., 2020. Evidence for Multiple Superposed
1240 Fluvial Deposits Within Reuyl Crater, Mars. Journal of Geophysical Research: Planets
1241 125, e2019JE006136. <https://doi.org/10.1029/2019JE006136>
1242 Warner, N.H., Gupta, S., Calef, F., Grindrod, P., Boll, N., Goddard, K., 2015. Minimum
1243 effective area for high resolution crater counting of martian terrains. Icarus 245, 198–
1244 240. <https://doi.org/10.1016/j.icarus.2014.09.024>
1245 Williams, R.M.E., Chidsey Jr, T.C., Eby, D.E., 2007. Exhumed paleochannels in central
1246 Utah—Analogues for raised curvilinear features on Mars, in: Hylland, M.D., Clark, D.L.,
1247 Chidsey, T.C. (Eds.), Central Utah - Diverse Geology of a Dynamic Landscape, Utah
1248 Geological Association Publication.
1249 Williams, R.M.E., Irwin, R.P., Burr, D.M., Harrison, T., McClelland, P., 2013. Variability in
1250 martian sinuous ridge form: Case study of Aeolis Serpens in the Aeolis Dorsa, Mars,
1251 and insight from the Mirackina paleoriver, South Australia. Icarus 225, 308–324.
1252 <https://doi.org/10.1016/j.icarus.2013.03.016>
1253